Cell Reports
Physical Science

CellPress
OPEN ACCESS

Article

A Robust Flow-Through Platform for Organic Contaminant Removal

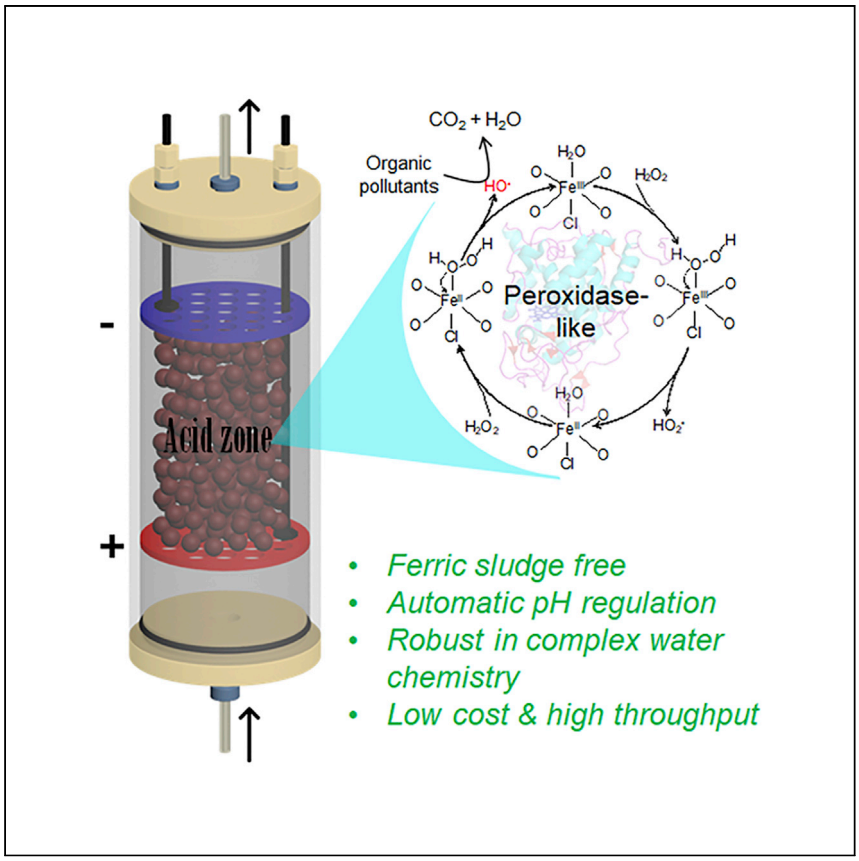

Clean water is a sustainable development goal of the United Nations, but it is threatened by toxic organic pollutants. Chen et al. aim to upgrade an advanced oxidation water treatment unit, using electricity to generate the strong acidity required by the Fenton process, providing a path to green water treatment.

Long Chen, Akram N. Alshawabkeh, Shayan Hojabri, Meng Sun, Guiyin Xu, Ju Li

a.alshawabkeh@northeastern.edu (A.N.A.)
xuguiyin@mit.edu (G.X.)
liju@mit.edu (J.L.)

HIGHLIGHTS

Electrochemical water splitting under flow-through conditions produces high acidity

This acidity boosts the Fenton-like catalytic activity for organic compound removal

Acidity is verified by modeling and experiment

Stability and robustness of this platform are demonstrated

Chen et al., Cell Reports Physical Science 2, 100296
January 20, 2021
https://doi.org/10.1016/j.xcrp.2020.100296

Cell Reports
Physical Science

CellPress
OPEN ACCESS

Article

A Robust Flow-Through Platform for Organic Contaminant Removal

Long Chen,[1] Akram N. Alshawabkeh,[1,*] Shayan Hojabri,[1] Meng Sun,[2] Guiyin Xu,[3,*] and Ju Li[3,4,5,*]

SUMMARY

Achieving the greatest cleanup efficiency with minimal footprint remains a paramount goal of the water treatment industry. Toxic organic compounds threaten drinking water safety and require effective pretreatment. Hydroxyl radicals produced by the Fenton process (Fe^{2+}/H_2O_2) destroy organic contaminants based on their strong oxidation potential. An upgraded reaction using solid catalysts, referred to as the Fenton-like process, was recently adopted to avoid the ferric sludge generation during the conventional Fenton process. However, most heterogeneous Fenton-like catalysts operate optimally at pH 3–5 and quite weakly in near-neutral water bodies. Here, we evaluate the feasibility of an electrolytically localized acid compartment (referred to as the *Ella* process) produced by electrochemical water splitting under flow-through conditions to facilitate the Fenton-like process. The *Ella* process boosts the activity of an immobilized iron oxychloride catalyst >10-fold, decomposing organic pollutants at a high flow rate. The robust performance in complex water bodies further highlights the promise of this platform.

INTRODUCTION

Various toxic organic compounds in the environment pose considerable threats to human health and the ecosystem. While efficient in providing clean drinking water, many advanced water treatment facilities have high capital and running costs that remain the principal barriers to implementation in developing countries.[1] The classic Fenton process, which transforms hydrogen peroxide (H_2O_2) into hydroxyl radicals ($HO^{\bullet}$) under the ferrous ions (Fe^{2+}) catalysis, is an affordable and proven water treatment technique.[2] $HO^{\bullet}$ is the second most oxidative species in nature after fluorine, with a redox potential of 2.73 V versus normal hydrogen electrode[2], and could non-selectively destroy recalcitrant organic contaminants in water.[3,4] By coupling with other water treatment units, such as coagulation, membrane filtration, or microbial degradation, the Fenton process can be adapted for various treatments of bodies of water.[5–7] Fruitful progress has been achieved to date in Fenton chemistry for water treatment.[8–12] In particular, *in situ* synthesis of H_2O_2 from H_2 and O_2 under noble metal catalysis[13] and H^+ and O_2 under photochemical[14] or electrochemical catalysis[11] are sustainable routes to reduce the chemicals cost. However, the formation of ferric sludge continues to be a challenge limiting implementation of the Fenton process. The sludge is formed when water pH is improved to approximately neutral after oxidation, and its toxicity stems from the adsorbed residual compounds in treated water.[15] Treatment of the ferric sludge requires substantial chemical and manpower costs—10% to 50% of the overall operating costs in a water treatment plant.[16,17]

[1]Department of Civil and Environmental Engineering, Northeastern University, Boston, MA 02115, USA

[2]Department of Chemical and Environmental Engineering, Yale University, New Haven, CT 06520-8286, USA

[3]Department of Nuclear Science and Engineering, Massachusetts Institute of Technology, Cambridge, MA 02139, USA

[4]Department of Materials Science and Engineering, Massachusetts Institute of Technology, Cambridge, MA 02139, USA

[5]Lead Contact

*Correspondence: a.alshawabkeh@northeastern.edu (A.N.A.), xuguiyin@mit.edu (G.X.), liju@mit.edu (J.L.)

https://doi.org/10.1016/j.xcrp.2020.100296

Heterogeneous solid catalysts could overcome the drawback of ferric sludge formation. Both naturally occurring clays/minerals and transition metal-centered designer composites have been extensively explored as Fenton-like catalysts.[8,18–21] These catalysts have noteworthy structural elegance in the unique coordination environment of their metal cores, which stabilizes the metal-H_2O_2 complex transition state and facilitates the electron transfer *inter se*.[22] Furthermore, the turnover of metal atoms on the catalyst surface occurs via a peroxidase-mimicking mechanism (see Figure S1 for peroxidase structure),[23] akin to the Haber-Weiss reaction of homogeneous Fenton chemistry.[24] The pH dependence of heterogeneous Fenton-like catalysts is generally less strict than that of free iron ions, the latter of which is the most effective at pH 2.8–3.5.[19] Nevertheless, most canonical Fenton-like catalysts favor acidic pH 3–5 (Table S1), and the catalyst turnover frequency (TOF) can be reduced by up to 100-fold under neutral conditions.[25,26] This is due to surface metal-OH complexes forming at higher pH values and repelling H_2O_2 away from the exposed active sites. However, pH regulation of near-neutral drinking water bodies is challenging, especially if the water contains high carbonate alkalinity; furthermore, the acidification of contaminated groundwater for *in situ* water treatment could release undesired metal ions from aquifers.[27,28] These concerns severely compromise the potential use of heterogeneous Fenton-like catalysts in the water treatment industry.

Flow electrochemistry holds great promise for automatic pH regulation to support water treatment, wherein OH^- and H^+ generated from the cathode and anode, respectively, are redistributed based on ion migration, dispersion, and hydraulic flux.[29] Here, we propose an electrolytically localized acidic-compartment (*Ella*) process to regulate solution pH for heterogeneous Fenton-like reactions, building on our extensive experiences in flow electrochemistry. The *Ella* process has a small footprint because it turns pH-neutral influent into acidic solution in between the electrodes, and zones beyond that are back to neutral as the influent. Combined with heterogeneous Fenton-like catalysts, the *Ella* process demonstrated excellent performance under long-term use, high flow rate, and complex water chemistry, manifesting the robustness of this coupled platform for recalcitrant organic compounds removal.

RESULTS AND DISCUSSION

Design of a Flow-Through Water Treatment Platform

The *Ella* process was used to regulate the pH of heterogeneous Fenton-like catalysts for water treatment with desired acidity. To this end, immobilized catalysts must be transferred to the acidic zone, whereby H_2O_2 is rapidly transformed into oxidizing $HO^{\bullet}$ radicals, leading to the instant degradation of organic compounds in the local vicinity (Figure 1A). This coupled water treatment process is categorized as an electro-Fenton-like (EFL) platform in this study. The flow-through treatment method is especially favored over the batch reaction mode for industry applications, since a water treatment plant treats high volumes of contaminated water at a fast pace. It is worth of noting that the EFL platform can take advantage of the intermittent solar and wind electricity, often with near-zero or even negative prices.

The contaminants treatment efficiency by the EFL platform is in the main determined by the reaction during the transport through the catalyst column—that is, longer retention times and higher catalyst and H_2O_2 concentrations tend to result in more complete contaminant removal. Therefore, the key aspects to warrant the success of the EFL platform are to promote $HO^{\bullet}$ generation and allow sufficient reaction time within the column.

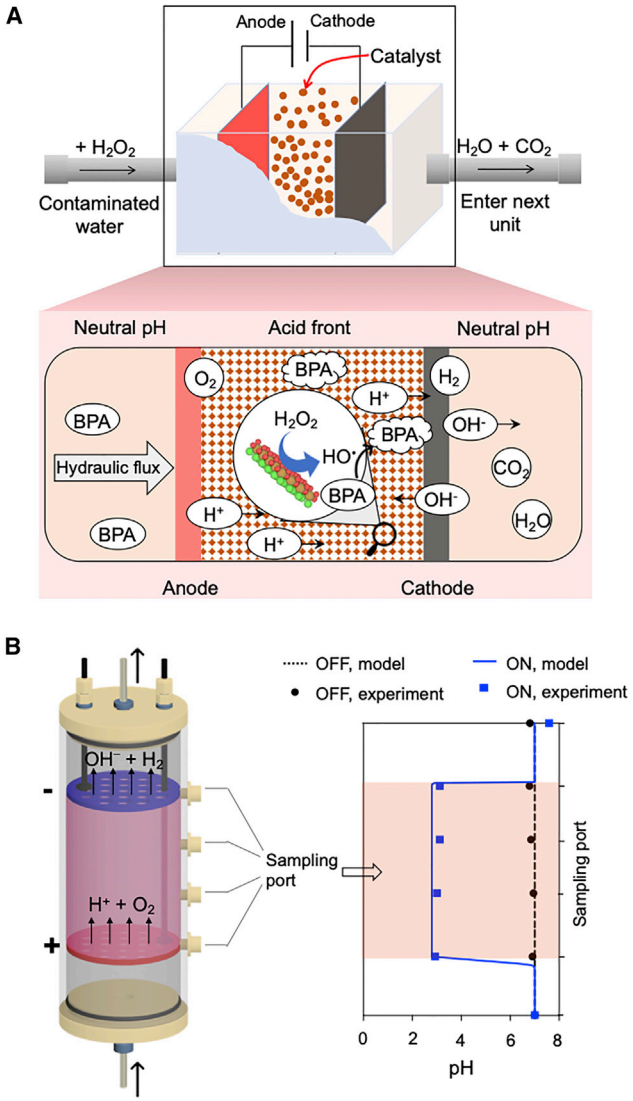

Figure 1. *Ella* Process-Based Flow-Through Water Treatment Platform

(A) Schematic representation of the flow-through platform. Placement of an anode upstream of a cathode produces an acid front, which promotes the activity of immobilized Fenton-like catalyst. The H_2O_2 is *in situ* transformed into $HO^•$ radical under catalysis, leading to oxidative mineralization of organic contaminant into CO_2 and H_2O. Bisphenol A (BPA) is used as a target compound for illustration purpose.

(B) Automatic pH regulation by the *Ella* process. The left panel depicts the setup configuration, and the right panel indicates the pH variation profile along the column axis as the applied electric current was turned off and on. Arrows indicate flow direction. + and - denote anode and cathode, respectively.

pH Regulation by the *Ella* Process

As a proof of concept, a benchtop flow-through device was manufactured for our EFL platform. A set of stable mixed metal oxide electrodes were installed 9 cm apart in a vertically anchored acrylic flow-through column device (15 cm × 5 cm outer diameter [OD]). The column was filled with clean silica sand (0.15–0.6 mm) to maintain a laminar flow. The combination of a 100-mA electric current and a 15-mL/min hydraulic flow rate was applied to the pH-neutral solution passing through the column, and solution pHs at various locations along the column were measured

(Figure 1B). The solution was homogeneously neutral without electric current; however, by turning on the 100-mA electric current, an acidic pH of 2.93–3.12 between the anode and cathode was automatically attained at steady state. The electrochemically created acidity is suitable for most Fenton-like catalysts. The effluent pH measured as 7.59 was close to the influent value (pH 7), showing minimal effect on the treated water pH. A reactive transport model (see Supplemental Experimental Procedures) that accounts for advection, hydrodynamic dispersion, and ion migration was used to simulate the pH profile.[30] Modeling results indicate that the theoretical acidity of the confined space between electrodes using the above stated experimental settings is pH 2.8. The slight discrepancy in pH between experimental results and modeled value is possibly due to the fact that the current efficiency of water electrolysis was not 100%.

Immobilization of Fenton-like Catalyst

Iron oxychloride (FeOCl) was reported to possess extraordinary Fenton-like catalytic activity with high fidelity and can be mass produced.[22,31] Characterizations of the synthetic FeOCl nanocatalyst produced via the calcination of $FeCl_3 \cdot 6H_2O$ were shown in Figures S2 and S3. Bisphenol A (BPA) was used as the primary pollutant to illustrate FeOCl catalytic degradation performance, as BPA is an environmental estrogen that disrupts the human endocrine system upon exposure.[32] A total of 10 μM BPA was rapidly degraded by the FeOCl/H_2O_2 reaction. However, the addition of ethanol, a strong $HO^{\bullet}$ radical quencher,[33] competed with BPA for the produced $HO^{\bullet}$ radical reservoir and fully inhibited BPA removal by the FeOCl/H_2O_2 reaction (Figure S4), demonstrating that the degradation of BPA was via $HO^{\bullet}$ radical (Note S1). It was further found that FeOCl showed optimal activity at pH 3, ~9.3-fold higher than that at pH 7 in terms of $HO^{\bullet}$ radical yield.

Density functional theory (DFT) calculation was harnessed to study the catalysis mechanism of the FeOCl/H_2O_2 reaction. It was revealed that the reaction is accomplished via two electron-transfer processes (Figure S5). In the first step, $Fe^{III}OCl$ is reduced by H_2O_2 into $Fe^{II}OCl$. In the second step, the derived $Fe^{II}OCl$ decomposes H_2O_2 into $HO^{\bullet}$ radical via homolytic cleavage. The readily reducible nature of unsaturated Fe atoms on the exposed (100) surface of FeOCl crystals allows rapid turnovers of $Fe^{III/II}$ to catalyze the H_2O_2 transformation. Specifically, the energy barrier of reducing Fe^{III} to Fe^{II} on FeOCl crystals by H_2O_2 was determined as 0.235 eV (Figure S6), whereas that of hematite (Fe_2O_3, a rhombohedral Fenton-like catalyst) is 0.76 eV as a comparison.[34]

It is, however, of great concern that the microcatalyst particles are subject to fluid transport, resulting in potential draining from the silica sand pores within the column device. For instance, by packing well-mixed FeOCl and silica sand particles into the column (Figure S7; Note S2), the overall catalyst activity decayed by 36% after 8 h due to hydraulic erosion (Figure S8). Another immobilization strategy of cross-linking FeOCl with alginate hydrogel was attempted for the effective retention of FeOCl nanoparticles (Figure S9; Note S3).[35] However, the resulting FeOCl/alginate composite showed only 1% activity compared to the same amount of unimmobilized FeOCl catalyst (Figure S10; Note S4), delivering poor in-reactor performance under high flow rates (Figures S11 and S12; Note S5). This is due to a large fraction of FeOCl particles becoming buried inside the hydrogel of the FeOCl/alginate composite and not being effectively accessible by H_2O_2 molecules.

To solve this problem, FeOCl nanoparticles were alternatively immobilized on a porous γ-Al_2O_3 support via a melt infiltration method[36] (Figure 2A), with the belief that this approach offers maximum FeOCl catalytic sites for H_2O_2 molecules. Field

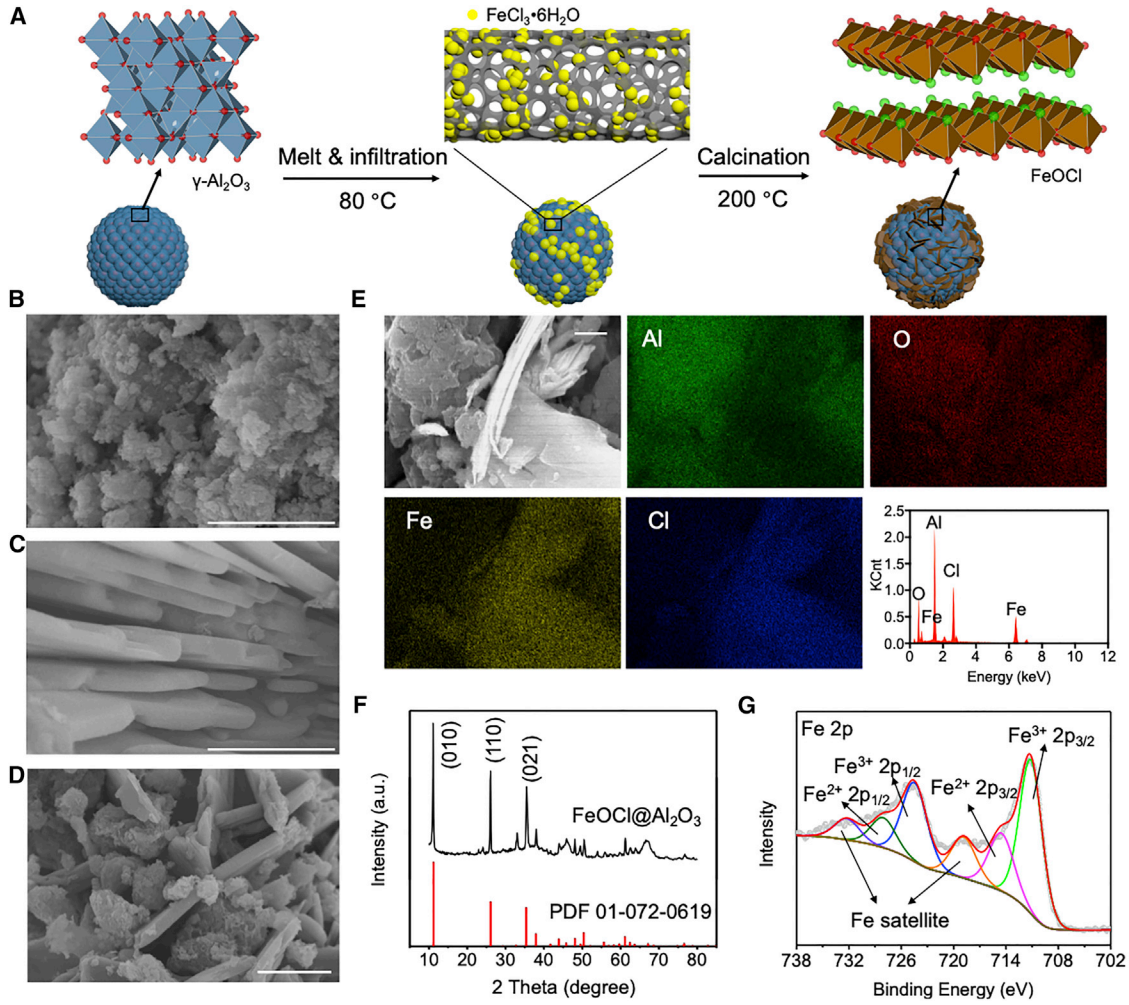

Figure 2. Immobilization of FeOCl onto γ-Al_2O_3 Support

(A) Illustration of melt infiltration strategy.

(B–D) SEM images of γ-Al_2O_3 (B), FeOCl (C), and FeOCl/Al_2O_3 (D).

(E) EDX element mapping and analysis of FeOCl/Al_2O_3.

(F) XRD pattern of FeOCl/Al_2O_3.

(G) Fe 2p deconvolution spectra of XPS analysis.

Scale bars indicate 1 μm.

emission scanning electron microscopy (FESEM) images clearly revealed the dispersion of FeOCl nanosheets on the amorphous γ-Al_2O_3 support in the synthesized FeOCl/Al_2O_3 composite (Figures 2B–2D), with a surface area of 206 m^2/g (Table S2). The compositional distribution of the FeOCl/Al_2O_3 was investigated with energy-dispersive X-ray spectroscopy (EDX) (Figure 2E). EDX analysis identified Al, O, Fe, and Cl elements on the FeOCl/Al_2O_3 composite. Elemental mapping results suggested that Al and Fe elements were separately located, in agreement with the overlay structure of the FeOCl/Al_2O_3 composite. Cl element exhibited a consistent pattern with Fe element on the FeOCl surface, while O element was uniformly distributed on the FeOCl/Al_2O_3 composite. X-ray diffraction (XRD) of the FeOCl/Al_2O_3 composite disclosed several characteristic diffraction peaks (2θ) at 11.2°, 26.1°, and 35.4°, which respectively belongs to the (010), (110), and (021) planes of the orthorhombic FeOCl crystal (Powder Diffraction File [PDF]: 01-072-0619) (Figure 2F). The chemical states of compositional elements were studied with X-ray

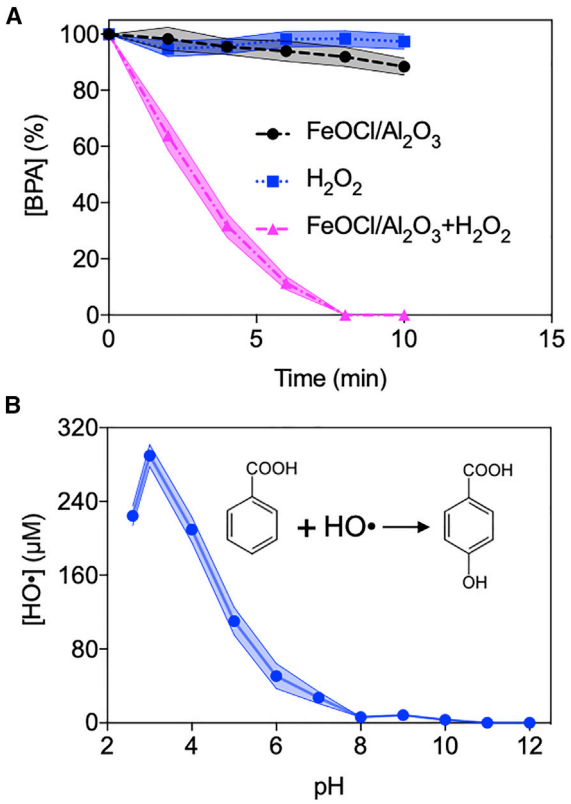

Figure 3. Catalytic Activity of $FeOCl/Al_2O_3$ Composite

(A) BPA degradation by $FeOCl/Al_2O_3$ and H_2O_2 reaction and controls. Reactions were performed at pH 3.

(B) Quantification of generated $HO^{\bullet}$ radical by $FeOCl/Al_2O_3$ and H_2O_2 reaction at different pH after reaction for 30 min. Inset shows the stoichiometric oxidation of benzoic acid for $HO^{\bullet}$ radical yield determination. Shaded area indicates the error range of obtained data.

photoelectron spectroscopy (XPS).[37] In particular, deconvoluted Fe 2p spectrum showed that Fe^{3+} $2p_{1/2}$ (724.6 eV) and $2p_{3/2}$ (711.2 eV) were dominant over Fe^{2+} $2p_{1/2}$ (728.2 eV) and $2p_{3/2}$ (714.6 eV) (Figure 2G), which is consistent with the unimmobilized FeOCl crystal (Figure S3). XPS analyses of other elements in the $FeOCl/Al_2O_3$ composite and the γ-Al_2O_3 support are shown in Figures S13 and S14. Overall, the results above suggested that the morphology and electronic properties of the FeOCl crystal remained intact after immobilization on the γ-Al_2O_3 support.

Activity test results of the synthetic $FeOCl/Al_2O_3$ composite are shown in Figure 3. It was found that 10 μM BPA was completely degraded in 10 min by 0.2 g/L $FeOCl/Al_2O_3$ and 10 mM H_2O_2 at pH 3, while the $FeOCl/Al_2O_3$ composite or H_2O_2 alone led to negligible BPA removals. Furthermore, under the stated conditions, $FeOCl/Al_2O_3$-mediated Fenton-like reaction produced the most remarkable amount of $HO^{\bullet}$ radicals at pH 3 (i.e., 289.8 μM after reaction for 30 min), the acidity of which could be readily achieved by the *Ella* process. The catalytic performance of the $FeOCl/Al_2O_3$ composite showed a pattern consistent with that of the unimmobilized FeOCl nanoparticle (Figure S4), indicating that the γ-Al_2O_3 support played no role in H_2O_2 transformation.

High Performance of the Electro-Fenton-like Platform

The synthetic $FeOCl/Al_2O_3$ composites were transferred to the space between electrodes of the column to use the acidity produced by the *Ella* process (Figure 4A).

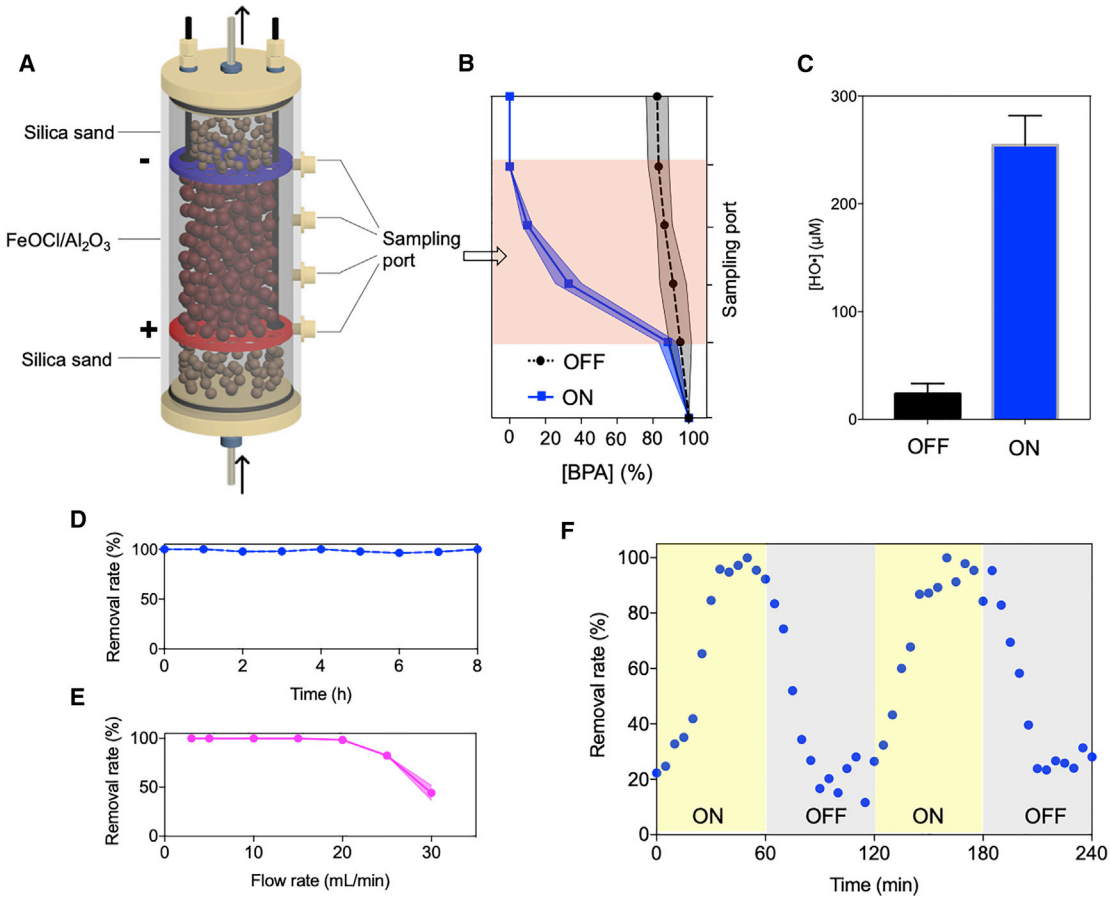

Figure 4. Performance of Electro-Fenton-like Platform

(A) Illustration of column device components.

(B and C) BPA removals from each sampling port (B), and (C) quantification of generated HO• radical by electro-Fenton-like platform as the electric current was turned off and on.

(D–F) Stability test (D), (E) tolerance of flow rate, and (F) electricity responsiveness assay of the electro-Fenton-like platform. Influent flow rate was subjected to change for (E). Arrows indicate flow direction. + and - denote anode and cathode, respectively.

Data in (C) are represented as means ± SEMs. Shaded areas in (B), (D), and (E) indicate the error range of obtained data.

Neutral solutions containing 10 mM H_2O_2 oxidant and 10 μM BPA contaminant were pumped through the column at a rate of 15 mL/min, and BPA removals along the hydraulic flux direction were measured (Figure 4B). Low BPA removal from the effluent (17.6%) was observed without electric current, due to the weak activity of FeOCl/Al_2O_3 under neutral condition. However, after a 100-mA electric current was applied to the electrodes, the gradual degradation of BPA took place as measured from the sampling ports, and BPA removal reached 100% in the effluent. Direct BPA degradation by electrodes was ruled out based on the control experiment without the FeOCl/Al_2O_3 catalyst (Figure S15). In addition, the presence of 10 mM ethanol as the HO• radical scavenger almost fully quenched BPA removal (Figure S15), suggesting that *in situ*-produced HO• radicals accounted for BPA degradation. As shown in Figure S16, the HO• radicals generated by the EFL platform could also non-selectively degrade other organic contaminants, including drugs (ibuprofen and carbamazepine), herbicide (atrazine), pesticide and drug precursors (4-chlorophenol and 4-nitrophenol), and recalcitrant dyes (rhodamine B, reactive blue 19, and orange II). The operating process to treat a dye solution may be viewed in more detail in Video S1. It was further determined that the yield of HO• radical produced by the

platform when the 100-mA electric current was turned off and on was 23.5 and 254.4 μM, respectively (Figure 4C). This 10.8-fold increase in $HO^{\bullet}$ radical production was attributed to the acidic environment created by the *Ella* process, which boosted the $FeOCl/Al_2O_3$ catalyst activity. The results indicate that the EFL platform, by coupling a heterogeneous Fenton-like catalyst and the *Ella* process in a flow-through column device, is effective for the removal of organic contaminants.

The long-term stability of BPA removal by the EFL platform was tested (Figure 4D). Over the course of 8-h reactions, laminar fluid transport was maintained, and the BPA removal steadily approached 100%. Clearly, a duration of 8 h is not enough for practical industry application, but here is used as a proof of concept to demonstrate the durability of our system at the current stage. Future studies will include longer tests of up to weeks. BPA removal by this platform under different hydraulic flow rates was also measured (Figure 4E). A high flow rate leads to shortened contact time among H_2O_2 molecules, the catalyst surface, and the organic contaminant, which reduces $HO^{\bullet}$ radical yield and compromises contaminant removal. Over 95% of 10 μM BPA could be removed from the effluent at a flow rate of <20 mL/min, whereas the BPA removal rate decreased to 82.4% and 44.4% at 25 and 30 mL/min, respectively. The tolerance of flow rate by using $FeOCl/Al_2O_3$ in this design was greatly superior to that using FeOCl crosslinked on alginate hydrogel as a catalyst (Figure S12), primarily due to the abundant catalytic sites exposed on the surface of the $FeOCl/Al_2O_3$ composite.

The responsiveness of BPA removal by the EFL platform to the electric current was monitored by repeatedly turning the electric power supply on and off, with a 60-min interval. As shown in Figure 4F, BPA removal significantly increased after the 100-mA electric current was turned on for 15 min, and approached 100% after 40 min. As the power was turned off, BPA removal gradually decreased during the first 30 min, from 84.3%–92.3% to 16.7%–23.9%, and was steady afterward. The non-instant response of BPA removal to electricity was presumably because of the slow accumulation and the desorption of protons. The results demonstrated that electricity is a critical governor of contaminant removal by our developed platform. In addition, the observed response time in this study matches well with the intermittency of solar or wind-generated renewable electricity, and therefore our device can provide clean drinking water without the need for battery energy storage.

Robustness against Complex Water Chemistry

Complex water environments are typically encountered in water treatment practices, posing challenges to downgradient treatment. For instance, water bodies receiving leachates from industries could be highly basic and require a pH neutralization process such as CO_2 sequestration before biological/chemical treatment.[38] In this study, contaminants in a synthetic basic solution are treated by the EFL platform. Influent solutions of pH 7–11 were effectively acidified to ~pH 3 under 100 mA electric current and a 15-mL/min flow rate, in good agreement with modeling results (Figure 5A). Consequently, BPA removals approached 100% under the *Ella* process-mediated acidic environment, regardless of influent pH, whereas <22.4% of BPA was removed when the electric current was turned off (Figure 5B).

The potential of water bodies to neutralize protons, namely water alkalinity, represents another challenge for acid-demanding chemical treatments due to the buffering carbonate ions, expressed as equivalent milligrams of $CaCO_3$/L.[39] Specifically, a substantial amount of acid is required to overcome high water alkalinity for the conventional Fenton process. BPA removal in synthetic solutions containing 0–200 mg

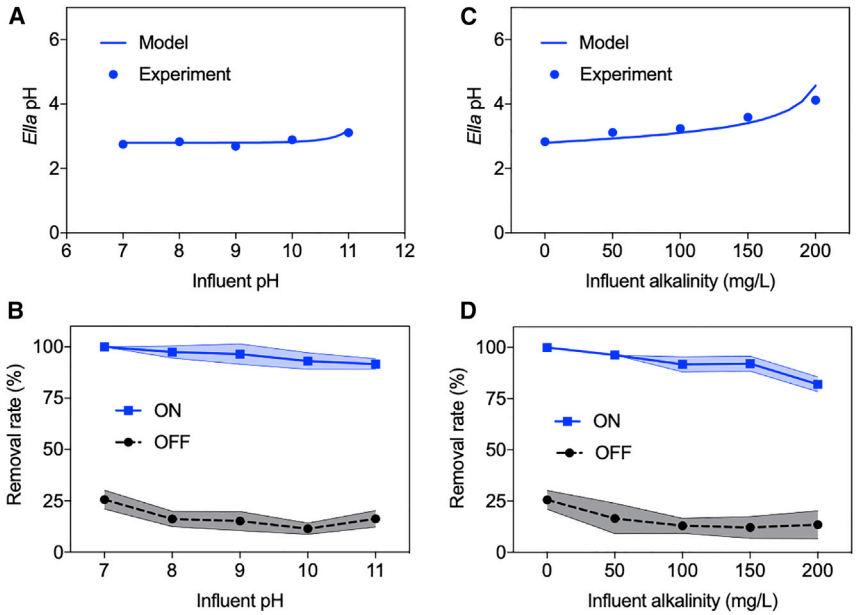

Figure 5. Robustness of Electro-Fenton-like Platform against Complex Water Chemistry

(A and C) Acidic pH produced by *Ella* process.

(B and D) BPA removals when the electric current was turned off and on.

(A and B) Influents were adjusted to different initial pHs, and (C and D) sodium carbonate was added to influents for synthetic alkalinity and influents were maintained at neutral. *Ella* pH denotes the average of solution pHs from 2 middle sampling ports. Shaded areas in (B) and (D) indicate the error range of obtained data.

$CaCO_3$/L water alkalinity was tested by the EFL platform. The results show that the solution of higher alkalinity was less prone to acidification by the *Ella* process, but the acidic zone was still below pH 4.14 in all of the tests under the 100-mA electric current and the 15-mL/min flow rate (Figure 5C). This acidity led to an 84.5%–100% removal efficiency of BPA, which is significantly higher than that when the electric current was turned off (Figure 5D). The acidity produced by the *Ella* process could be tuned against the water buffering capacity by adjusting the applied electric current and hydraulic flow rate. For instance, a combination of 60 mA electric current and 2 mL/min flow rate is able to acidify a solution of 500 mg $CaCO_3$/L alkalinity from pH 8 to pH 3.5.[40]

Test with Field Water Samples

The results demonstrate the effectiveness of the EFL platform in synthetic solutions of complex water chemistry. Furthermore, in this study, water samples extracted in the field from surface or groundwater sources were used as the matrices for BPA removal, with intrinsic conductivity supporting electrochemical water splitting. Water-quality characteristics are shown in Table S4. Treated water bodies were acidified to pH 2.9–4.04 by the *Ella* process, and 91.7%–97.2% BPA removals were achieved by the mediated Fenton-like process (Figure S17).

Techno-economic Analysis

Compared with the conventional Fenton process, the required energy for electrochemical water splitting by this integral EFL platform is estimated to be 1.39 kWh/m^3 influent, which translates into a cost of \$0.091/m^3 based on the average US industrial electricity rate (\$0.0653/kWh).[41] This value is subjected to optimization based

on applied electric current, hydraulic flow rate, and solution conductivity, but it only constitutes ~10% of unit operating costs by modern water treatment plants.[42] The cost of γ-Al_2O_3 and $FeCl_3 \cdot 6H_2O$ is estimated at \$0.5/kg[43] and \$0.3/kg,[44] respectively. This means it takes <\$0.0005 to synthesize 1 g $FeOCl/Al_2O_3$ catalyst, and we used ~50 g of synthesized catalyst particles for our device. By considering the long-term stability of this catalyst, its cost is indeed negligible. Furthermore, *in situ* electrochemical synthesis of highly concentrated H_2O_2[45,46] could be used as a replacement for externally supplied H_2O_2 in the future, eliminating the chemical cost.

Conventional Fenton reactions produce a tremendous amount of iron sludge, which needs treatment and induces huge costs. The cost of sludge disposal post-water treatment is ~\$40–\$100/ton.[16,52] However, the total cost is unclear since different amounts of iron are used for different bodies of water. Nevertheless, it has been reported that the cost for treating sludge is 10%–50% of the total cost, and sometimes can be up to 60%.[17] Therefore, we believe the overall cost of our system is lower than conventional Fenton reactions. Our design avoids the iron sludge generation, which not only reduces the cost but also is more environmentally friendly. In general, however, the techno-economic analysis here is quite preliminary and will require more in-depth work in the future.

Moreover, we would like to mention future directions of scaling up the device. First, the catalyst should be cheap and easy to produce. One can certainly replace FeOCl with other Fenton catalysts, such as the nano MnO_2 catalyst,[53,54] since our system is not solely dependent on the FeOCl. Second, to ensure sufficient contact time between H_2O_2 and catalyst, the two electrodes should be distant enough. An outcome of this design strategy is the high voltage applied onto the two electrodes to drive the migration of proton and other ions. This will eventually increase the cost in electricity, and hence there exists a "sweet spot" where electricity cost and catalysis performance reach a trade-off balance. Finally, the immobilization of the FeOCl catalyst should be adapted for industrial-scale operation. For example, it has been widely reported that catalyst nanoparticles could be ground into large particles via ball milling.[55–57] This scalable method leads to very stable catalyst immobilization.

The EFL water treatment platform developed in this study shows the potential for practical implementation by the water treatment industry after upscaling. The fast response of the EFL platform in removing organic pollutants especially allows for smart controls at low cost. In addition, it possesses the easy-to-(un)install feature that makes it affordable and compatible with other connecting units of a centralized water treatment facility. For instance, a feasible niche of this device is to function as an electrochemical filter before advanced purification units requiring the removal of fouling hazards such as organic molecules and biofilm-forming bacteria.[47,48] On the small size end, our EFL platform can be redesigned to provide clean drinking water for individual families without using the electrical grid, by coupling with cheap photovoltaic sources.

Here in this work, an EFL platform wherein an electrochemically produced acidic environment supports the heterogeneous Fenton-like reaction was developed for a high-throughput water treatment purpose. This integrated platform relies on an electrolytically localized acid compartment, referred to as the *Ella* process. The acidic pH produced by the *Ella* process (100 mA electric current and 15 mL/min flow rate) mediated a 10.8-fold increase in $HO^{\bullet}$ yield, which contributes to the complete removal of contaminants in the effluent. The EFL platform shows strong

stability for long-term use, tolerance of high water flux, and effectiveness against complex water chemistry for organic contaminant removal. The proposed setup configuration is advantageous in that it provides a high degree of automation that enables water treatment by controlling the electric power, and also in the low operating cost that most modern water treatment plants strive for, both of which are especially attractive for industrial applications.

EXPERIMENTAL PROCEDURES

Resource Availability

Lead Contact

Requests for further information and resources and reagents can be directed to the Lead Contact, Prof. Ju Li (liju@mit.edu)

Materials Availability

This study did not generate new unique reagents.

Data and Code Availability

The authors declare that the data supporting the findings of this study are available within the article and the Supplemental Information. All other data are available from the Lead Contact upon reasonable request.

Chemicals

$FeCl_3 \cdot 6H_2O$ (Honeywell Fluka) was used to synthesize the FeOCl nanocatalyst, and H_2O_2 was purchased from Fisher Scientific. γ-Al_2O_3 (Alfa Aesar) was used as a support to immobilize FeOCl. BPA (Sigma-Aldrich), ibuprofen (Alfa Aesar), atrazine (Sigma-Aldrich), carbamazepine (Sigma-Aldrich), 4-chlorophenol (Acros Organics), 4-nitrophenol (Acros Organics), rhodamine B (Harleco), reactive blue 19 (Sigma-Aldrich), and orange II (Acros Organics) were used as substrates for the Fenton-like process treatment. Other chemicals (i.e., sodium sulfate [Na_2SO_4] as the supporting electrolyte, sodium carbonate [Na_2CO_3] for synthetic alkaline water, ethanol as a $HO^{\bullet}$ radical scavenger, and methanol and acetonitrile as the mobile phase for high-performance liquid chromatography [HPLC]) were purchased from Fisher Scientific. Pure water was used throughout the work, except in the field water studies.

Synthesis of FeOCl

A total of 2 g ground $FeCl_3 \cdot 6H_2O$ powder was put at the bottom of a ceramic crucible and then tightly sealed with aluminum foil. The crucible was heated at an 8°C/min rate up to 200°C and maintained for 2 h in a muffle furnace. After heating, the crucible was naturally cooled down to room temperature. The cooling process took ~1 h. The formed dark red FeOCl plates were ground into fine powder and then washed with ethanol at least three times until the eluent was colorless to remove residual $FeCl_3$ impurity. Eventually, the synthesized and purified FeOCl was stored in a dry 15-mL Corning tube, and then put in a chemical fume hood under constant ventilation drying.

Synthesis of FeOCl/Al_2O_3

A total of 10 g ground γ-Al_2O_3 microparticles were mixed with 5.97 g $FeCl_3 \cdot 6H_2O$ (i.e., theoretical 10 wt% Fe loading) under vigorous vortex for 10 min until the powder mixture turned homogeneously yellow. The powder was then transferred into 5-mL glass tubes with air-tight caps and further sealed with Teflon bands to prevent the vaporization of crystalline water in $FeCl_3 \cdot 6H_2O$. The glass tubes were heated under 80°C for 12 h, during which $FeCl_3 \cdot 6H_2O$ (melting point 37°C) infiltrated the γ-Al_2O_3 pores. The obtained powder was transferred into crucibles for the synthesis of

$FeOCl/Al_2O_3$ using the same conditions as FeOCl synthesis. Produced $FeOCl/Al_2O_3$ was extensively washed with ethanol before use.

Characterization of Materials

The crystalline phase of samples was measured using a D/MAX-2200 XRD analyzer equipped with a rotation anode using CuKα radiation (λ = 0.1541 nm). FESEM photography was performed on an S-4800 instrument at an accelerating voltage of 15 kV. High-resolution transmission electron microscopy (HRTEM) images were obtained on a JEOL JEM-2100F transmission electron microscope at an accelerating voltage of 200 kV. The chemical composition and the binding states on the surface of the FeOCl specimen were carried out on a Thermo Scientific ESCALAB 250 Xi XPS microprobe with monochromatic X-ray (Al Kα, 1,486.6 eV) radiation as an excitation source. The measurements of specific surface area, pore volume, and pore size distribution in the 2–500 nm range were carried out using a Micromeritics ASAP 2020 instrument by nitrogen adsorption/desorption at 77.3 K (−194.85°C).

Flow-through Column Reaction

The experimental column (15 × 5 cm OD, 0.32 cm wall thickness) is made with cast acrylic tubes and Teflon rods with O-rings as the top and bottom caps. Mixed metal oxide sintered titanium (Ti/MMO, IrO2:RuO2 50:50 mixture deposited on titanium substrate) mesh electrodes were inserted parallel to one another at a distance of 9 cm. Titanium hex nuts and threaded rods were used to connect Ti/MMO electrodes with the electric power source. Gum rubber was sealed on the external titanium rod to prevent contact with both electrodes. Four sampling ports using tube adaptors (0.79375 cm tube to 0.3175 cm National Pipe Tapered [NPT] male) were installed at an equal distance (3 cm) between the electrodes.

To load catalysts into the reactor, the $FeOCl/Al_2O_3$ catalyst (~50 g) was filled between the cathode and anode, and rest spaces were filled with fine silica sand particles. The silica sand particles were extensively washed with pure water and then oven dried at 80°C. Filter papers were placed at the bottom and top of the sand zones to prevent particles from draining into the effluent.

Initially, a neutral solution (pH 7) of 10 μM BPA was used to condition the column until the effluent BPA concentration matched the influent to reach adsorption equilibrium. After BPA breakthrough, another neutral solution containing 10 mM H_2O_2, 10 μM BPA, and 5 mM Na_2SO_4 electrolyte was pumped up by a peristaltic pump into the vertically aligned column at a rate of 15 mL/min, with a 100-mA electric current applied to the electrodes. A steady-state acid compartment was formed between electrodes after 60 min, and BPA removal was tested. One-milliliter solutions sampled from each port and influent/effluent were neutralized with 1 mL 20 mM phosphate buffer (pH 7) to avoid following analysis inaccuracy due to pH inconsistence. Samples after filtration with the 0.45 μm polyvinylidene fluoride (PVDF) membrane (13 mm diameter, Jin Teng) were measured by HPLC (Agilent 1200 Infinity Series) equipped with an Agilent Eclipse AAA C18 column (4.6 × 150 mm). BPA was separated by 0.5 mL/min methanol/water 60/40 mobile phase and detected at 228 nm wavelength using the Agilent 1260 diode array detector. The degradation of other substrates was also tested, and quantification methods are indicated in Table S3.

In certain assays, the solution pH, flow rate, and synthetic alkalinity (i.e., 1 mM Na_2CO_3 is equivalent to 100 mg $CaCO_3$/L water alkalinity) were subjected to changes, as indicated, while other parameters were fixed, as stated above. For

the electricity responsiveness test, an experiment was initiated by turning on the 100-mA electric current after conditioning the column, without reaching steady state. For BPA removal in field water bodies, water samples 1 and 2 were taken from lakes in Boston, Massachusetts, and water samples 3 and 4 were taken from underground sources of Superfund sites in Puerto Rico. They were stored in a 4°C cold room. Characterizations of the field water samples are shown in Table S4. Water samples were filtrated through 0.45 μm PVDF membranes (47 mm diameter, EMD Millipore) before use to remove suspended particles. Solution pH was not adjusted after the addition of H_2O_2 and BPA, and solution intrinsic conductivity supported electrochemical water splitting. BPA concentrations in the influent and effluent were analyzed during steady state.

Hydroxyl Radical Quantification Method

The total $HO^{\bullet}$ radical amount was quantified via a reported benzoic acid oxidation method.[49] Briefly, the accumulated $HO^{\bullet}$ radical amount equals that of generated *p*-hydroxybenzoic acid, a product of $HO^{\bullet}$ radical and benzoic acid reaction, multiplied by a conversion factor of 5.87. In the batch reaction, 100 mL solutions of 5 mM benzoic acid, 10 mM H_2O_2, and 0.2 g/L catalyst (i.e., free FeOCl or immobilized FeOCl/Al_2O_3) were stirred for 30 min under the indicated solution pH. In the flow-through reaction, after conditioning the column with 5 mM benzoic acid until breakthrough, influent solutions containing 5 mM benzoic acid, 10 mM H_2O_2, and 5 mM Na_2SO_4 at neutral pH passed through the column at a rate of 15 mL/min, with or without the 100-mA electric current applied to the electrodes. Effluent samples were collected during steady state. The concentration of generated *p*-hydroxybenzoic acid was analyzed by HPLC with the mobile phase of 0.5 mL/min methanol/water 20/80 and the detection wavelength at 255 nm using the same column for BPA analysis.

DFT Calculation Method

Geometry Optimization. DFT calculations were performed with PBE (Perdew-Burke-Ernzerhof) functional by using CASTEP[50,51] as incorporated in Materials Studio 7.0. The ultrasoft pseudopotential (USPP) was used to represent the core-valence electron interaction. The plane wave expansion basis sets with a cutoff energy of 300 eV was used. The k-point sampling of 4 × 4 × 2 within the Monkhorst-Pack special k-point scheme in the Brillouin zone was considered for geometry optimization and energy calculation.

Transition State Calculation. To investigate the pathways of the Fenton process, linear synchronous transit/quadratic synchronous transit (LST/QST) by using the DFT+*U* technique were performed, and the *U* values of O 2p and Fe 3d are 6.3 and 3.0 eV, respectively. The FeOCl (100) surface was considered a reactive surface with 2 fixed atomic layers,[40] and 2 × 2 × 1 k-point mesh was used. Spin polarization was considered for all of the calculations.

SUPPLEMENTAL INFORMATION

Supplemental Information can be found online at https://doi.org/10.1016/j.xcrp.2020.100296.

ACKNOWLEDGMENTS

This work was financially supported by the US National Institute of Environmental Health Sciences (NIEHS, grant no. P42ES017198). J.L. acknowledges support from the NSF (ECCS-1610806). We would like to thank Michael MacNeil and Kurt Braun

for column reactor fabrication. We appreciate the DFT calculation by Hao Chen and Mingguang Chen, and valuable discussion with Dr. Yunfei Xue on catalyst immobilization. The content is solely the responsibility of the authors and does not necessarily represent the official views of the NIEHS.

AUTHOR CONTRIBUTIONS

L.C., A.N.A., G.X., and J.L. conceived the study. L.C. and G.X. performed the study and analyzed the data. S.H. developed the reactive transport model. All of the authors participated in writing and reviewing the manuscript.

DECLARATION OF INTERESTS

The authors intend to file a patent for this work, and they declare no other competing interests.

Received: July 24, 2020
Revised: October 29, 2020
Accepted: December 1, 2020
Published: January 20, 2021

REFERENCES

1. Lu, L., Guest, J., Peters, C., Zhu, X., Rau, G., and Ren, Z. (2018). Wastewater treatment for carbon capture and utilization. Nat. Sustain. *1*, 750–758.

2. Wardman, P. (1989). Reduction potentials of one-electron couples involving free radicals in aqueous solution. J. Phys. Chem. Ref. Data *18*, 1637–1755.

3. Babuponnusami, A., and Muthukumar, K. (2014). A review on Fenton and improvements to the Fenton process for wastewater treatment. J. Environ. Chem. Eng. *2*, 557–572.

4. Pignatello, J.J., Oliveros, E., and MacKay, A. (2006). Advanced oxidation processes for organic contaminant destruction based on the Fenton reaction and related chemistry. Crit. Rev. Environ. Sci. Technol. *36*, 1–84.

5. Feng, F., Xu, Z., Li, X., You, W., and Zhen, Y. (2010). Advanced treatment of dyeing wastewater towards reuse by the combined Fenton oxidation and membrane bioreactor process. J. Environ. Sci. (China) *22*, 1657–1665.

6. Wu, Y., Zhou, S., Ye, X., Chen, D., Zheng, K., and Qin, F. (2011). Transformation of pollutants in landfill leachate treated by a combined sequence batch reactor, coagulation, Fenton oxidation and biological aerated filter technology. Process Saf. Environ. *89*, 112–120.

7. Ganiyu, S.O., Van Hullebusch, E.D., Cretin, M., Esposito, G., and Oturan, M.A. (2015). Coupling of membrane filtration and advanced oxidation processes for removal of pharmaceutical residues: a critical review. Separ. Purif. Tech. *156*, 891–914.

8. Herney-Ramirez, J., Vicente, M.A., and Madeira, L.M. (2010). Heterogeneous photo-Fenton oxidation with pillared clay-based catalysts for wastewater treatment: a review. Appl. Catal. B *98*, 10–26.

9. Pouran, R., Aziz, A.A., and Daud, W. (2015). Review on the main advances in photo-Fenton oxidation system for recalcitrant wastewaters. J. Ind. Eng. Chem. *21*, 53–69.

10. Bokare, A.D., and Choi, W. (2014). Review of iron-free Fenton-like systems for activating H_2O_2 in advanced oxidation processes. J. Hazard. Mater. *275*, 121–135.

11. Brillas, E., Sirés, I., and Oturan, M.A. (2009). Electro-Fenton process and related electrochemical technologies based on Fenton's reaction chemistry. Chem. Rev. *109*, 6570–6631.

12. Ganiyu, S.O., Zhou, M., and Martínez-Huitle, C.A. (2018). Heterogeneous electro-Fenton and photoelectro-Fenton processes: a critical review of fundamental principles and application for water/wastewater treatment. Appl. Catal. B *235*, 103–129.

13. Yi, Y., Wang, L., Li, G., and Guo, H. (2016). A review on research progress in the direct synthesis of hydrogen peroxide from hydrogen and oxygen: noble-metal catalytic method, fuel-cell method and plasma method. Catal. Sci. Technol. *6*, 1593–1610.

14. Moon, G., Fujitsuka, M., Kim, S., Majima, T., Wang, X., and Choi, W. (2017). Eco-friendly photochemical production of H_2O_2 through O_2 reduction over carbon nitride frameworks incorporated with multiple heteroelements. ACS Catal. *7*, 2886–2895.

15. Bolobajev, J., Kattel, E., Viisimaa, M., Goi, A., Trapido, M., Tenno, T., and Dulova, N. (2014). Reuse of ferric sludge as an iron source for the Fenton-based process in wastewater treatment. Chem. Eng. J. *255*, 8–13.

16. Pliego, G., Zazo, J.A., Blasco, S., Casas, J.A., and Rodriguez, J.J. (2012). Treatment of highly polluted hazardous industrial wastewaters by combined coagulation–adsorption and high-temperature Fenton oxidation. Ind. Eng. Chem. Res. *51*, 2888–2896.

17. Neyens, E., and Baeyens, J. (2003). A review of classic Fenton's peroxidation as an advanced oxidation technique. J. Hazard. Mater. *98*, 33–50.

18. Garrido-Ramírez, E.G., Theng, B.K.G., and Mora, M.L. (2010). Clays and oxide minerals as catalysts and nanocatalysts in Fenton-like reactions—a review. Appl. Clay Sci. *47*, 182–192.

19. Cheng, M., Lai, C., Liu, Y., Zeng, G., Huang, D., Zhang, C., Qin, L., Hu, L., Zhou, C., and Xiong, W. (2018). Metal-organic frameworks for highly efficient heterogeneous Fenton-like catalysis. Coord. Chem. Rev. *368*, 80–92.

20. Munoz, M., De Pedro, Z.M., Casas, J.A., and Rodriguez, J.J. (2015). Preparation of magnetite-based catalysts and their application in heterogeneous Fenton oxidation–a review. Appl. Catal. B *176*, 249–265.

21. Pouran, S.R., Raman, A.A.A., and Daud, W.M.A.W. (2014). Review on the application of modified iron oxides as heterogeneous catalysts in Fenton reactions. J. Clean. Prod. *64*, 24–35.

22. Sun, M., Chu, C., Geng, F., Lu, X., Qu, J., Crittenden, J., Elimelech, M., and Kim, J. (2018). Reinventing Fenton chemistry: iron oxychloride nanosheet for pH-insensitive H_2O_2 activation. Environ. Sci. Technol. Lett. *5*, 186–191.

23. Gao, L., Zhuang, J., Nie, L., Zhang, J., Zhang, Y., Gu, N., Wang, T., Feng, J., Yang, D., Perrett, S., and Yan, X. (2007). Intrinsic peroxidase-like activity of ferromagnetic nanoparticles. Nat. Nanotechnol. *2*, 577–583.

24. Koppenol, W.H. (2001). The Haber-Weiss cycle–70 years later. Redox Rep. *6*, 229–234.

25. Liu, S., Lu, F., Xing, R., and Zhu, J.J. (2011). Structural effects of Fe_3O_4 nanocrystals on peroxidase-like activity. Chemistry *17*, 620–625.

26. André, R., Natálio, F., Humanes, M., Leppin, J., Heinze, K., Wever, R., Schröder, H.C., Müller, W.E.G., and Tremel, W. (2011). V_2O_5 nanowires with an intrinsic peroxidase-like activity. Adv. Funct. Mater. *21*, 501–509.

27. Keith, C.D., Runnells, D.D., Esposito, J.K., Chermak, A.J., Levy, B.D., Hannula, R.S., Watts, M., and Hall, L. (2001). Geochemical models of the impact of acidic groundwater and evaporative sulfate salts on Boulder Creek at Iron Mountain, California. Appl. Geochem. *16*, 947–961.

28. Nordstrom, D.K., and Alpers, C.N. (1999). Negative pH, efflorescent mineralogy, and consequences for environmental restoration at the Iron Mountain Superfund site, California. Proc. Natl. Acad. Sci. USA *96*, 3455–3462.

29. Acar, Y.B., and Alshawabkeh, A.N. (1993). Principles of electrokinetic remediation. Environ. Sci. Technol. *27*, 2638–2647.

30. Hojabri, S., Rajic, L., and Alshawabkeh, A.N. (2018). Transient reactive transport model for physico-chemical transformation by electrochemical reactive barriers. J. Hazard. Mater. *358*, 171–177.

31. Yang, X.J., Xu, X.M., Xu, J., and Han, Y.F. (2013). Iron oxychloride (FeOCl): an efficient Fenton-like catalyst for producing hydroxyl radicals in degradation of organic contaminants. J. Am. Chem. Soc. *135*, 16058–16061.

32. Vandenberg, L.N., Hauser, R., Marcus, M., Olea, N., and Welshons, W.V. (2007). Human exposure to bisphenol A (BPA). Reprod. Toxicol. *24*, 139–177.

33. Adams, G.E., Boag, J.W., and Michael, B.D. (1965). Reactions of the hydroxyl radical. Part 2.-Determination of absolute rate constants. Trans. Faraday Soc. *61*, 1417–1424.

34. Ji, X.X., Wang, H.F., and Hu, P.J. (2019). First principles study of Fenton reaction catalyzed by FeOCl: reaction mechanism and location of active site. Rare Met. *38*, 783–792.

35. Smidsrød, O., and Skjåk-Braek, G. (1990). Alginate as immobilization matrix for cells. Trends Biotechnol. *8*, 71–78.

36. Eggenhuisen, T.M., den Breejen, J.P., Verdoes, D., de Jongh, P.E., and de Jong, K.P. (2010). Fundamentals of melt infiltration for the preparation of supported metal catalysts. The case of Co/SiO_2 for Fischer-Tropsch synthesis. J. Am. Chem. Soc. *132*, 18318–18325.

37. Xu, G., Yu, D., Zheng, D., Wang, S., Xue, W., Cao, X.E., Zeng, H., Xiao, X., Ge, M., Lee, W.K., and Zhu, M. (2020). Fast heat transport inside lithium-sulfur batteries promotes their safety and electrochemical performance. iScience *23*, 101576.

38. Gomes, H.I., Mayes, W.M., Rogerson, M., Stewart, D.I., and Burke, I.T. (2016). Alkaline residues and the environment: a review of impacts, management practices and opportunities. J. Clean. Prod. *112*, 3571–3582.

39. Lahav, O., and Birnhack, L. (2007). Quality criteria for desalinated water following post-treatment. Desalination *207*, 286–303.

40. Yuan, S., Chen, M., Mao, X., and Alshawabkeh, A.N. (2013). A three-electrode column for Pd-catalytic oxidation of TCE in groundwater with automatic pH-regulation and resistance to reduced sulfur compound foiling. Water Res. *47*, 269–278.

41. EIA (2020). Electric power monthly. Table 5.6.A. US average price of electricity to ultimate customers by end-use sector. https://www.eia.gov/electricity/monthly/epm_table_grapher.php?t=epmt_5_6_a.

42. Guo, T., Englehardt, J., and Wu, T. (2014). Review of cost versus scale: water and wastewater treatment and reuse processes. Water Sci. Technol. *69*, 223–234.

43. Intratec (2020). Aluminum oxide prices. Current & historical data in several countries. https://www.intratec.us/chemical-markets/aluminum-oxide-price.

44. Independent Commodity Intelligence Services (2020). US ferric chloride producers raise prices in healthy market. https://www.icis.com/explore/resources/news/2001/08/27/145944/us-ferric-chloride-producers-raise-prices-in-healthy-market/.

45. Chen, Z., Chen, S., Siahrostami, S., Chakthranont, P., Hahn, C., Nordlund, D., Dimosthenis, S., Nørskov, K.J., Bao, Z., and Jaramillo, F.T. (2017). Development of a reactor with carbon catalysts for modular-scale, low-cost electrochemical generation of H_2O_2. React. Chem. Eng. *2*, 239–245.

46. Yamanaka, I., Onizawa, T., Takenaka, S., and Otsuka, K. (2003). Direct and continuous production of hydrogen peroxide with 93 % selectivity using a fuel-cell system. Angew. Chem. Int. Ed. Engl. *42*, 3653–3655.

47. Guo, W., Ngo, H.H., and Li, J. (2012). A mini-review on membrane fouling. Bioresour. Technol. *122*, 27–34.

48. Gao, W., Liang, H., Ma, J., Han, M., Chen, Z., Han, Z., and Li, G. (2011). Membrane fouling control in ultrafiltration technology for drinking water production: a review. Desalination *272*, 1–8.

49. Zhou, X., and Mopper, K. (1990). Determination of photochemically produced hydroxyl radicals in seawater and freshwater. Mar. Chem. *30*, 71–88.

50. Clark, S.J., Segall, D.M., Pickard, J.C., Hasnip, J.P., Probert, I.J.M., Refson, K., and Payne, C.M. (2005). First principles methods using CASTEP. Z. Kristallogr. Cryst. Mater. *220*, 567–570.

51. Segall, M.D., Lindan, P.J.D., Probert, M.J., Pickard, C.J., Hasnip, P.J., Clark, S.J., and Payne, M.C. (2002). First-principles simulation: ideas, illustrations and the CASTEP code. J. Phys. Condens. Matter *14*, 2717–2744.

52. Neo Water Treatment (2020). Wastewater treatment disposal costs. https://neowatertreatment.com/wastewater-treatment-disposal-costs/.

53. Li, L., Du, Z., Liu, S., Hao, Q., Wang, Y., Li, Q., and Wang, T. (2010). A novel nonenzymatic hydrogen peroxide sensor based on MnO_2/graphene oxide nanocomposite. Talanta *82*, 1637–1641.

54. Xu, B., Ye, M.L., Yu, Y.X., and Zhang, W.D. (2010). A highly sensitive hydrogen peroxide amperometric sensor based on MnO_2-modified vertically aligned multiwalled carbon nanotubes. Anal. Chim. Acta *674*, 20–26.

55. Meng, X., Bi, X., Yu, C., Chen, G., Chen, B., Jing, Z., and Zhao, P. (2018). Ball-milling synthesized hydrotalcite supported Cu–Mn mixed oxide under solvent-free conditions: an active catalyst for aerobic oxidative synthesis of 2-acylbenzothiazoles and quinoxalines. Green Chem. *20*, 4638–4644.

56. Guo, X., Wang, Q., Xu, T., Wei, K., Yin, M., Liang, P., Huang, X., and Zhang, X. (2020). One-step ball milling-prepared nano Fe_2O_3 and nitrogen-doped graphene with high oxygen reduction activity and its application in microbial fuel cells. Front. Environ. Sci. Eng. *14*, 30.

57. Zhou, J., Zhang, M., and Zhu, Y. (2015). Photocatalytic enhancement of hybrid C_3N_4/TiO_2 prepared via ball milling method. Phys. Chem. Chem. Phys. *17*, 3647–3652.

Cell Reports Physical Science, Volume *2*

Supplemental Information

A Robust Flow-Through Platform for Organic Contaminant Removal

Long Chen, Akram N. Alshawabkeh, Shayan Hojabri, Meng Sun, Guiyin Xu, and Ju Li

Supplemental Experimental Procedures

Reactive transport model to estimate the steady-state pH in the *Ella* process

Water splitting is considered as the dominant electrolysis reaction in this system. This process will produce an acid front after the anode and gets neutralized after passing through the cathode.

$$\text{Anode: } 2H_2O \rightarrow O_2 + 4H^+ + 2e^- \quad (1)$$

$$\text{Cathode: } 2H_2O + 2\,e^- \rightarrow H_2 + 2OH^- \quad (2)$$

Competing reactions may exist depending on the electrolyte composition and concentration which reduces the current efficiency of the system. However, in this study we assume 100% efficiency for water electrolysis on both electrode surfaces.

Transport process in the column is expressed by Nernst-Plank's equation in dilute electrolytes.

$$J_i = uC_i - D_{H_i}\nabla C_i - u_i z_i F C_i \nabla\phi \quad (3)$$

Where u is the pore water velocity and J_i, C_i, D_{H_i}, u_i, and z_i are the total flux, concentration, hydrodynamic dispersion coefficient, mobility, and the charge of i^{th} species, respectively. Species mobility, u_i, can be estimated by Einstein relation.

$$u_i = \frac{z_i F D_i}{RT} \quad (4)$$

Hydrodynamic dispersion, D_H, is a function of the pore water velocity and is represented as $D_H = \tau D_0 + \alpha_L u$, where the tortuosity, τ, is a measure of effective transport path through media, D_0, is the molecular diffusion coefficient, and α_L, is the longitudinal

dispersivity. Many studies are conducted to evaluate the hydrodynamic dispersion coefficient[1]. This factor in large scale systems is estimated by column tracer test or fitted models of similar experiment characteristics.

In systems with supporting electrolyte, migration term can be neglected. Therefore, the governing equation for a transient simulation is obtained by conservation of mass.

$$\frac{\partial C_i}{\partial t} = -\nabla J_i + R_i \tag{5}$$

Where R_i is the reaction rate of species i in the bulk fluid. Electric field in the electrolyte can be calculated considering conservation of charge in the electrolyte, knowing that current arises from the motion of all charged species.

$$i = -\kappa \nabla\phi - \kappa F \sum_i z_i D_i \nabla C_i \tag{6}$$

Where the first term is ohmic potential and the second term is concentration-caused potential. In systems with supporting electrolyte, the concentration gradient can be neglected and the equation reduces to

$$i = -\kappa \nabla\phi \tag{7}$$

Where

$$\kappa = F^2 \sum_i z_i^2 u_i C_i \tag{8}$$

The inlet boundary condition is considered Dirichlet boundary with a constant feed concentration over time.

$$C(x = 0, t) = C_0 \tag{9}$$

The outlet boundary condition is a Neumann boundary condition:

$$\nabla C_i = 0 \tag{10}$$

Fluxes on the surface of the electrodes are shown as followed.

$$J_i|_{x=electrode+\partial x} = J_i|_{x=electrode-\partial x} + J_{eRXN,i} \tag{11}$$

where, $J_{eRXN,i}$, is the inward electrochemical source/sink flux for i^{th} species and is calculated in a constant current operating condition using Faraday's law.

$$J_{eRXN,i} = \frac{I}{z_i FA} \tag{12}$$

I applied current

z_i number of electrons participating for each mole of species i produced/consumed

F Faraday's constant, $96485\ c/eq$

A Electrode surface area

The homogeneous phase reactions included in the model are assumed to reach equilibrium.

$$\sum_{j=1}^{N_c} v_{ij} C_j = 0 \qquad \text{for } i = 1, \dots, N_x \tag{13}$$

N_c total number of species

N_x total number of reactions

v_{ij} stochiometric constant for j^{th} species in the i^{th} reaction

There have been many studies on integration of species transport and equilibrium reaction models[2-6]. In this study, reaction simulations and species concentrations are determined by PHREEQC computer program[7]. PHREEQC is a computer program which

is designed and optimized for aqueous geochemical reactions with a strong database. Nardi et al. have developed a comprehensive geochemical model using COMSOL Multiphysics for transport calculations and PHREEQC for geochemical reaction calculations[8]. Paz Garcia et al.[5] have obtained a similar approach in simulation of electrochemical remediation reactors using COMSOL Multiphysics with an interface with PHREEQC. In our study, we used MATLAB as the main platform for numerical calculation with an interface with PHREEQC for chemical reaction calculations. The interface written in MATLAB is used to transfer data between MATLAB and PHREEQC using Microsoft COM (Component Object Model). *Phreeqc.dat* is the thermodynamic database used in this study for equilibrium calculations. The reactions in the bulk fluid include acid/base reactions, water association/dissociation reaction, and redox reactions. Due to the characteristics of the aqueous reactions in this system, local equilibrium is considered.

In this study, hybrid Finite Volume differencing scheme is used for spatial discretization and implicit scheme is used for temporal discretization with a non-iterative sequential solver for integration of reactions in the simulation. This scheme guarantees continuity of the concerned variables and stability of numerical simulation. The hybrid scheme will evaluate the differencing scheme based on local Peclet number.

$$Pe = \frac{u}{D/L} \tag{14}$$

If the local Peclet number is small, diffusion is dominant and central differencing scheme results in smaller error. However, if the advection is dominant, upwind scheme is used to more accurately capture the impact of advection[9].

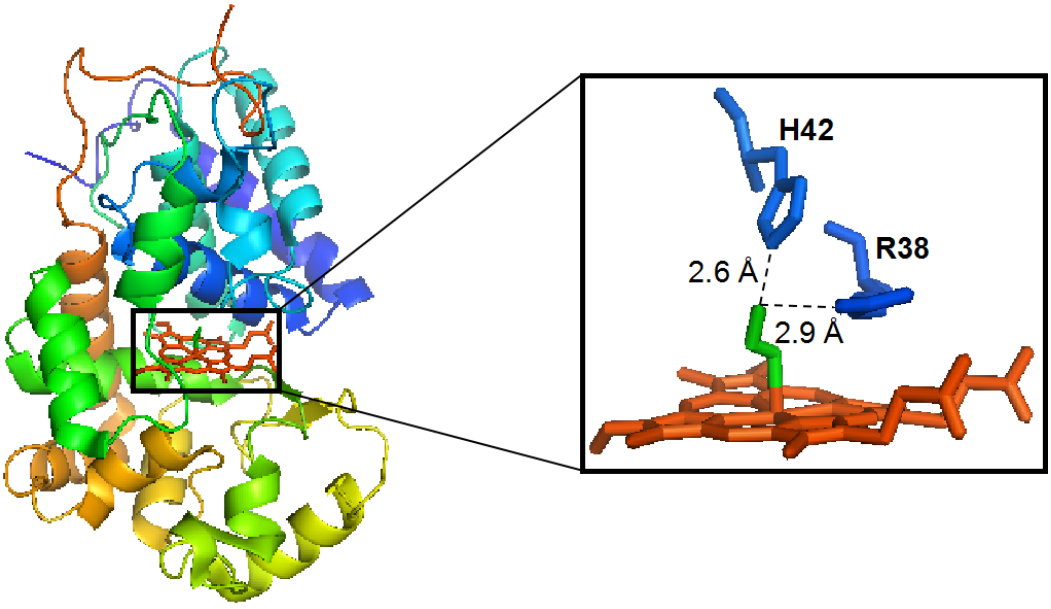

Figure S1. Horseradish peroxidase (HRP) protein structure (PDB entry: 1W4W). Right panel: formate as an allosteric inhibitor binds to the iron atom of heme compound, and this complex is stabilized by H42 and R38 of HRP peptide.

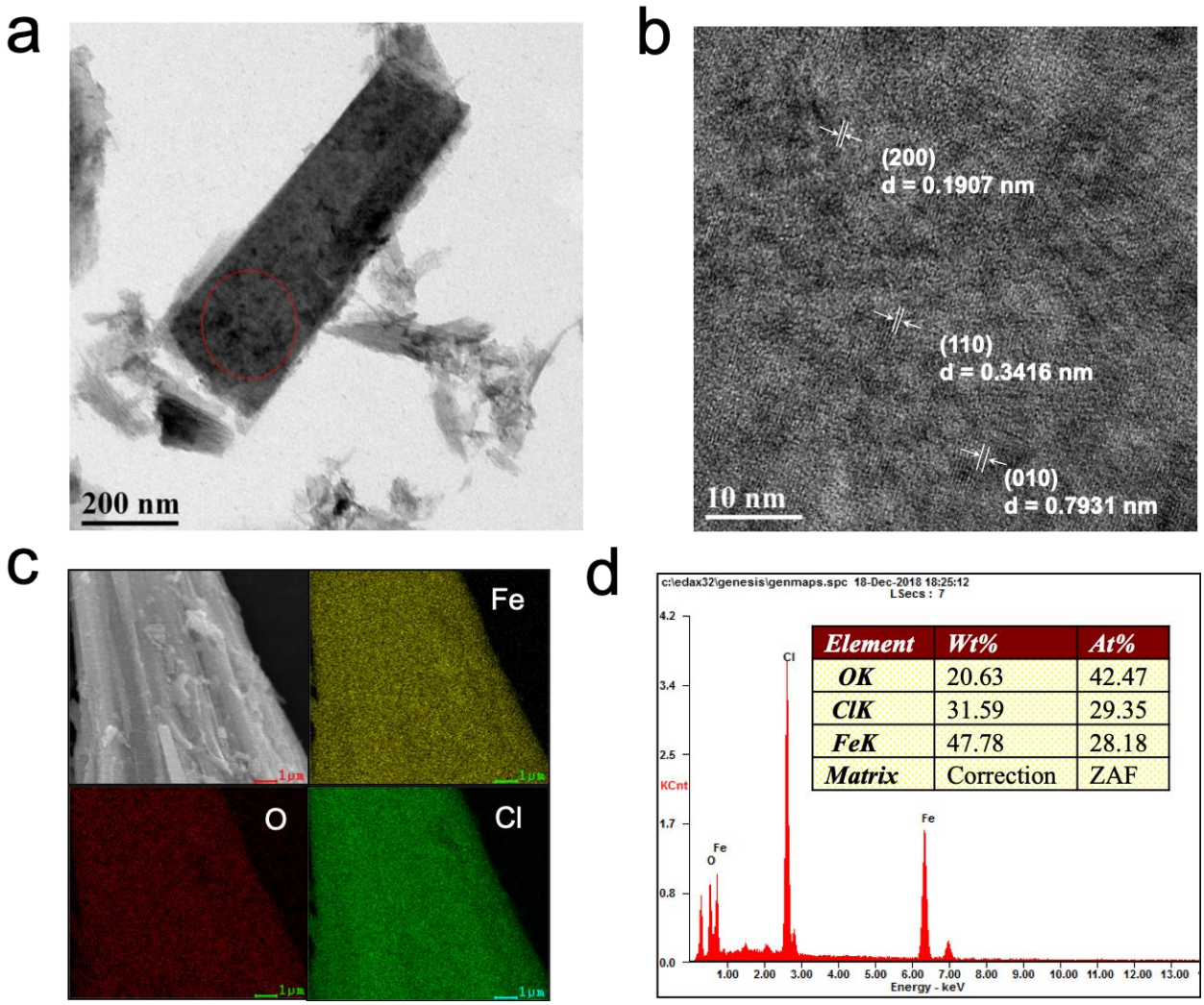

Figure S2. Characterizations of synthesized FeOCl nanosheet catalyst. (**a**) TEM, (**b**) HRTEM, (**c**) element mapping and (**d**) element ratio measurement from EDX analysis.

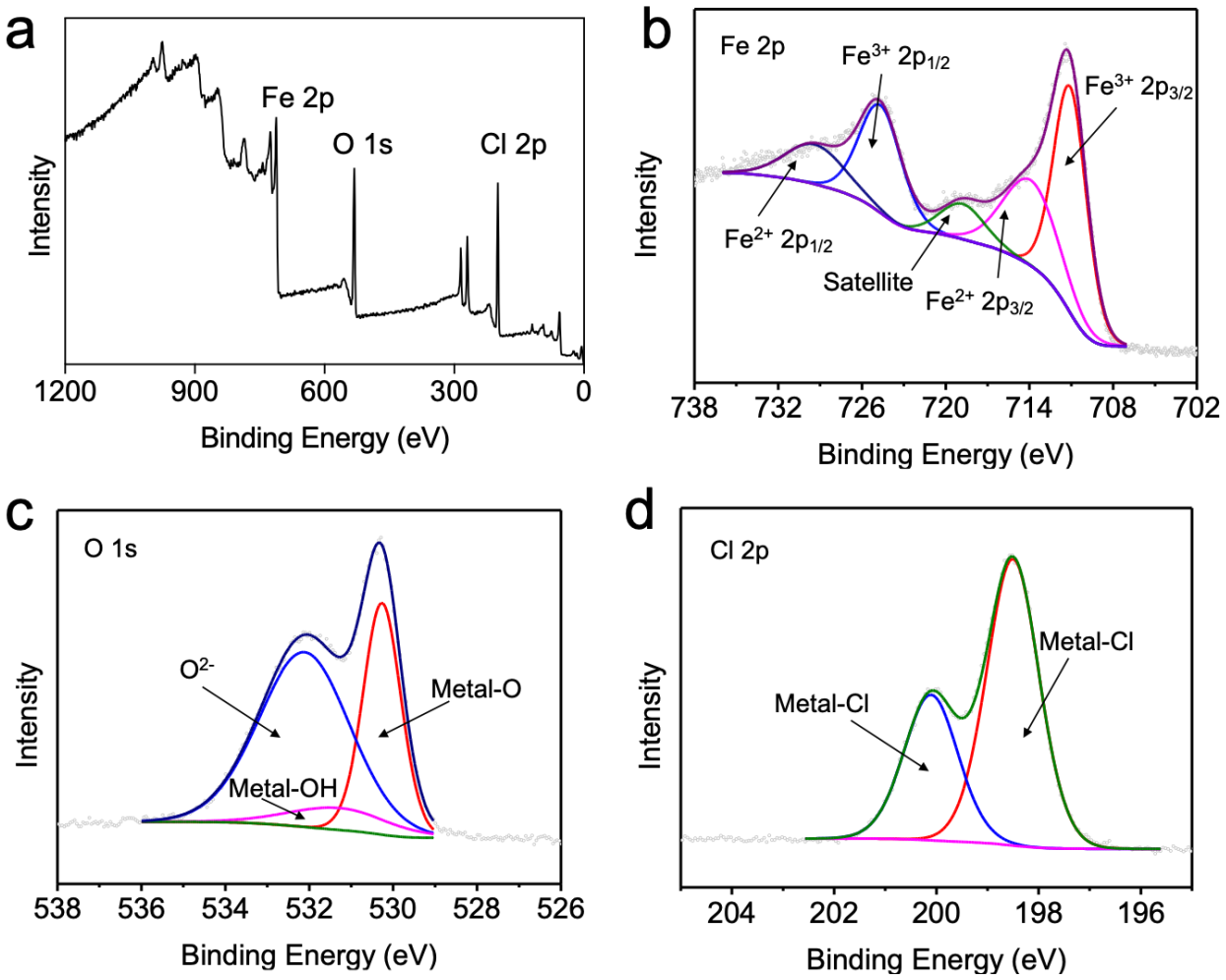

Figure S3. XPS characterization of FeOCl sample. (**a**) Survey spectrum, (**b**) Fe 2p, (**c**) O 1s, and (**d**) Cl 2p.

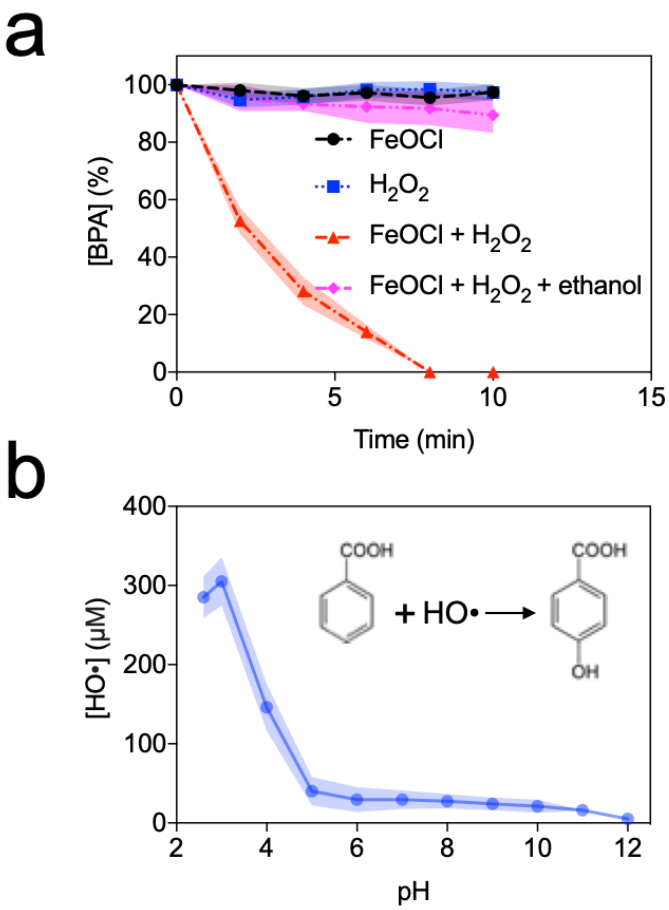

Figure S4. Activity of synthesized FeOCl. (**a**). BPA degradation by FeOCl/H_2O_2 reaction. (**b**). Quantification of generated HO• radical by FeOCl/H_2O_2 reaction at different pH.

Note S1. The activity of synthesized FeOCl sample was tested by decomposing H_2O_2 for BPA removal. It was shown that 0.2 g/L FeOCl with 10 mM H_2O_2 at pH 3 could remove 86% 10 μM BPA in 6 min and 100% BPA in 8 min. The role of HO• radical in BPA removal was verified by ethanol as a scavenger, since it fully inhibited BPA removal via quenching HO• radical. The catalytic activities of FeOCl at different pHs were compared. Results showed that, the optimum pH for FeOCl is around pH 3 as it mediated the highest yield of HO• radical.

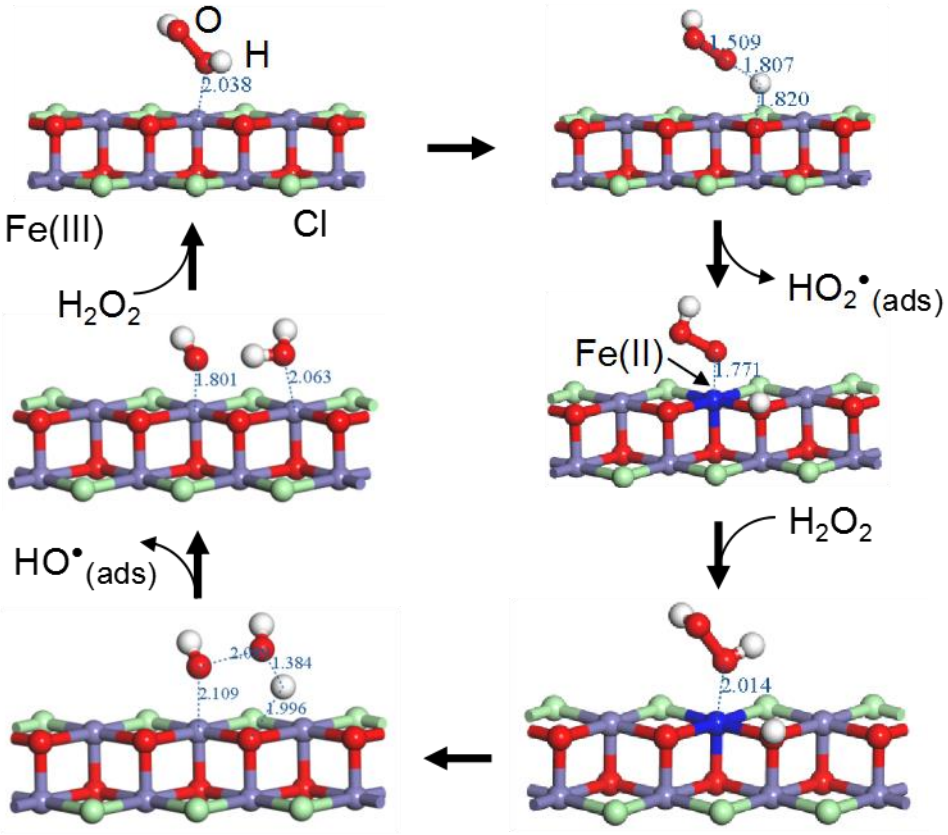

Figure S5. Peroxidase-like catalysis mechanism of FeOCl/H_2O_2 reaction.

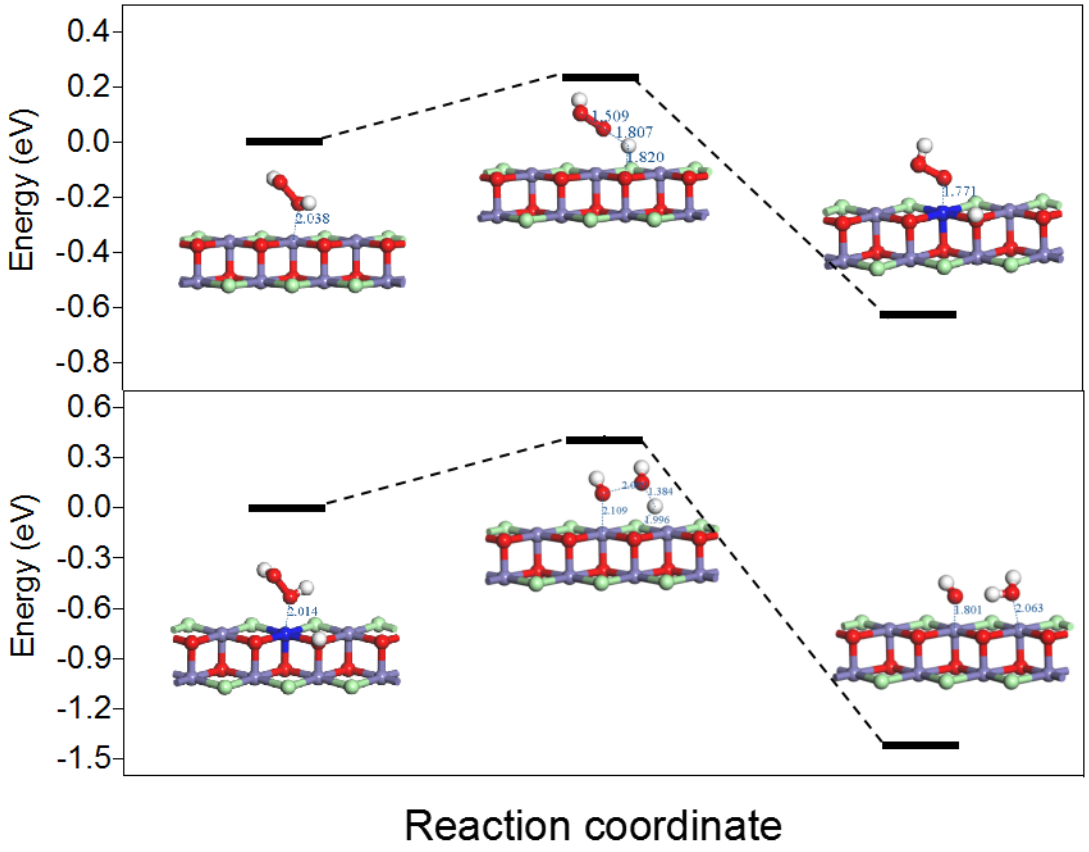

Figure S6. Reaction energy in step 1 (top) and step 2 (bottom) based on DFT calculation. Step 1: $Fe^{III}OCl$ is at first reduced by H_2O_2 into $Fe^{II}OCl$, and Step 2: the derived $Fe^{II}OCl$ then decomposes H_2O_2 into $HO^{\bullet}$ radical via homolytic cleavage.

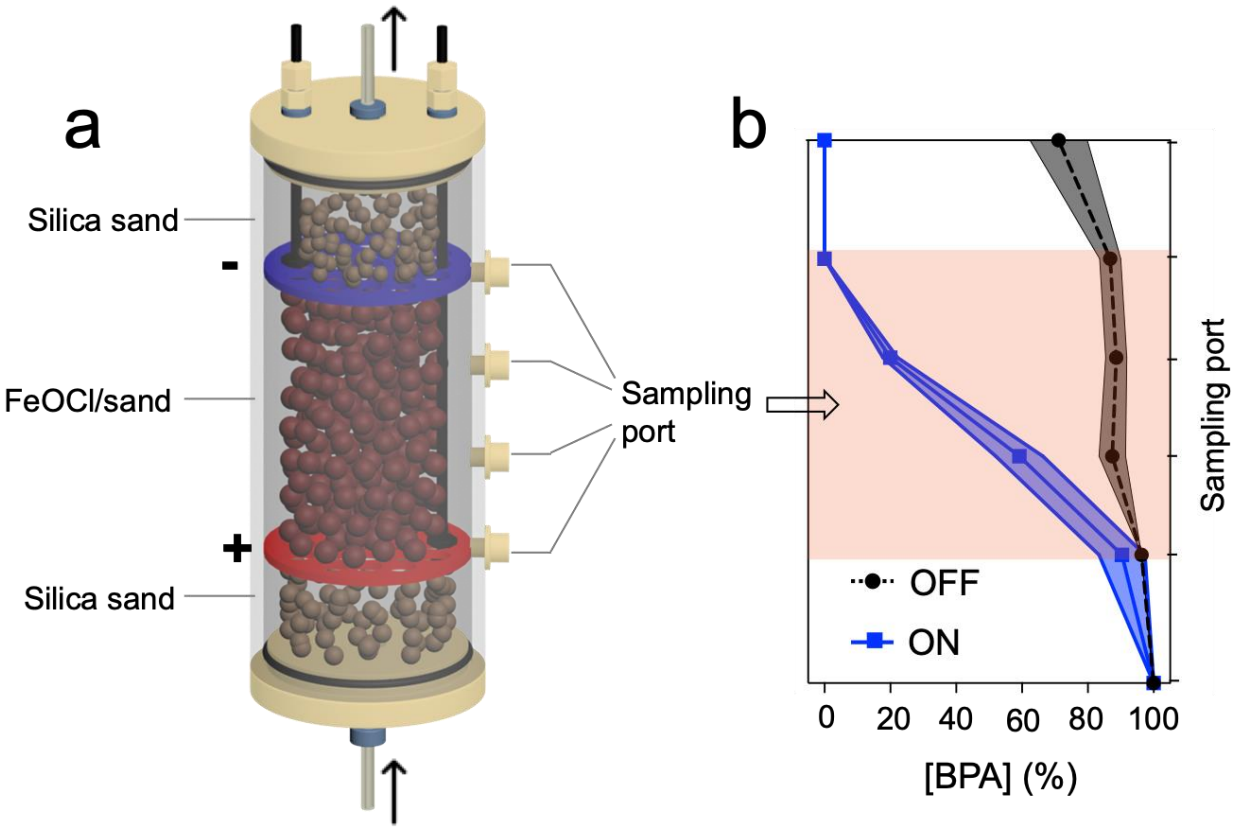

Figure S7. BPA removal by EFL platform loading unimmobilized FeOCl. (**a**). Illustration of reactor components, (**b**). BPA removals from each sampling port as the electric current was turned on and off.

Note S2. 5 g FeOCl powder was mixed well with 50 g sand particles under vortex for 20 min, and the mixture was then filled in between the cathode and anode, and all other spaces were filled with sand particles to reduce hydrodynamic perturbation. A neutral solution containing 10 mM H_2O_2, 10 μM BPA, and 5 mM Na_2SO_4 as electrolyte was pumped up into the vertically aligned reactor at a rate of 15 mL/min. A steady-state acidic-compartment was formed between the cathode and anode under a current of 100 mA after 60 min, and BPA removals at each sampling port was tested.

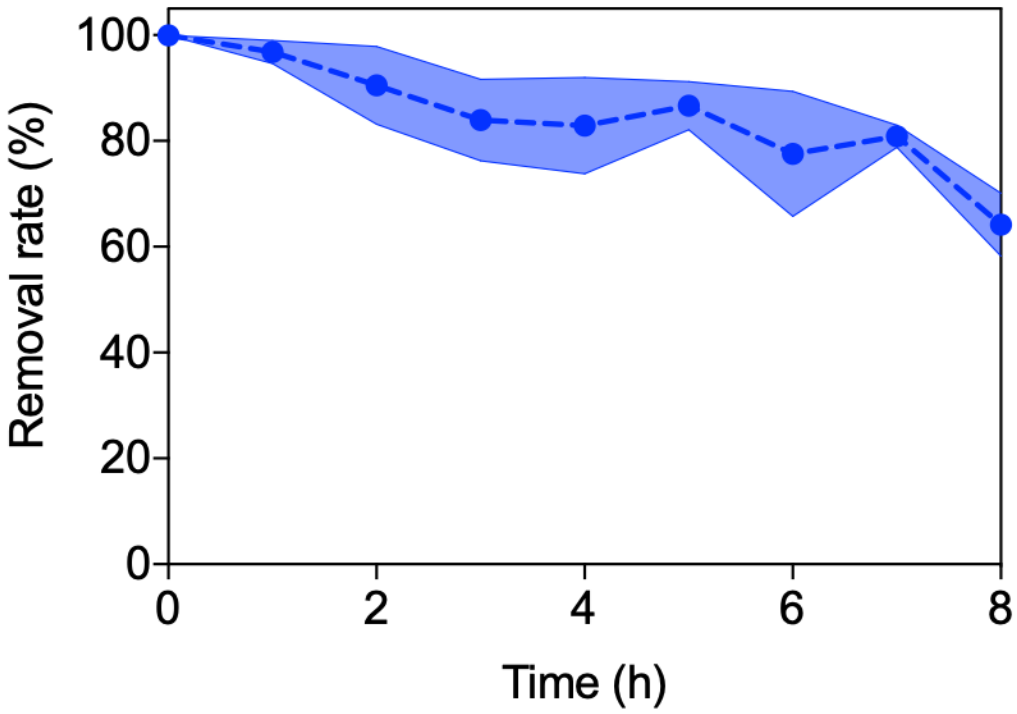

Figure S8. Stability test of BPA removal by reactor loading unimmobilized FeOCl (shown in **Fig. S7a**) for 8 h.

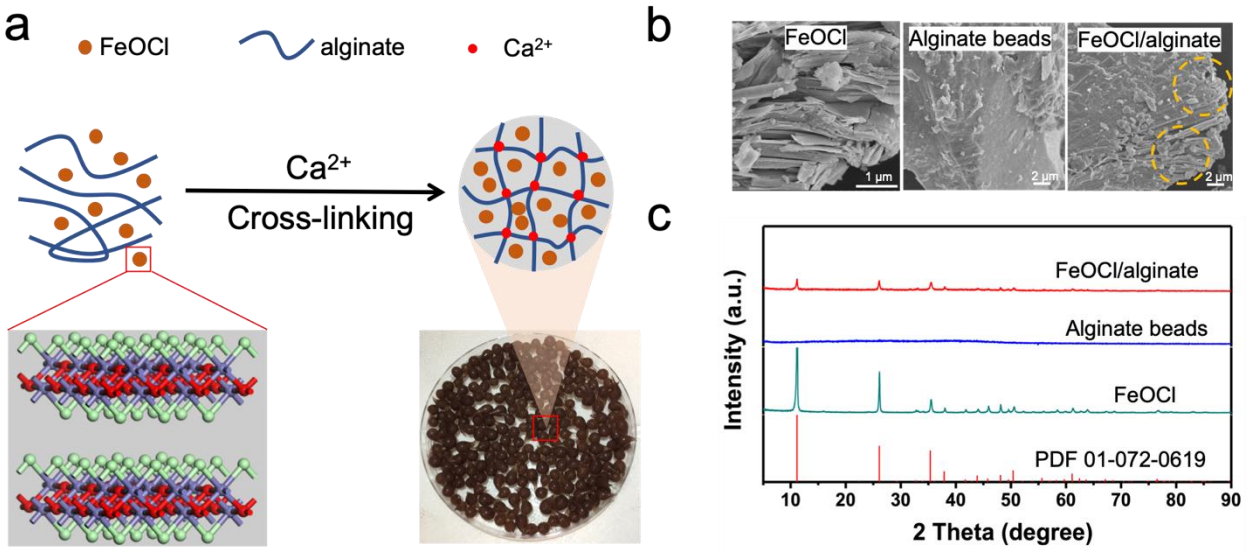

Figure S9. Immobilization of FeOCl on alginate hydrogel. (a) Illustration of immobilization strategy, (**b**) SEM and (**c**) XRD characterizations.

Note S3. 1.5 g synthesized FeOCl and 3 g alginate were at first sufficiently mixed via vigorous vortex, and then 100 mL DI water was poured into the beaker containing well-mixed FeOCl and alginate. A clean glass stick was used to stir the solution until it turned into homogeneous red paste. A syringe was then used to drop the red slurry into 0.1 M $CaCl_2$ solution, and formed FeOCl/alginate beads were allowed to harden for 2 h. The as-prepared FeOCl/alginate beads were then washed with DI water and loaded into the reactor for subsequent experiments.

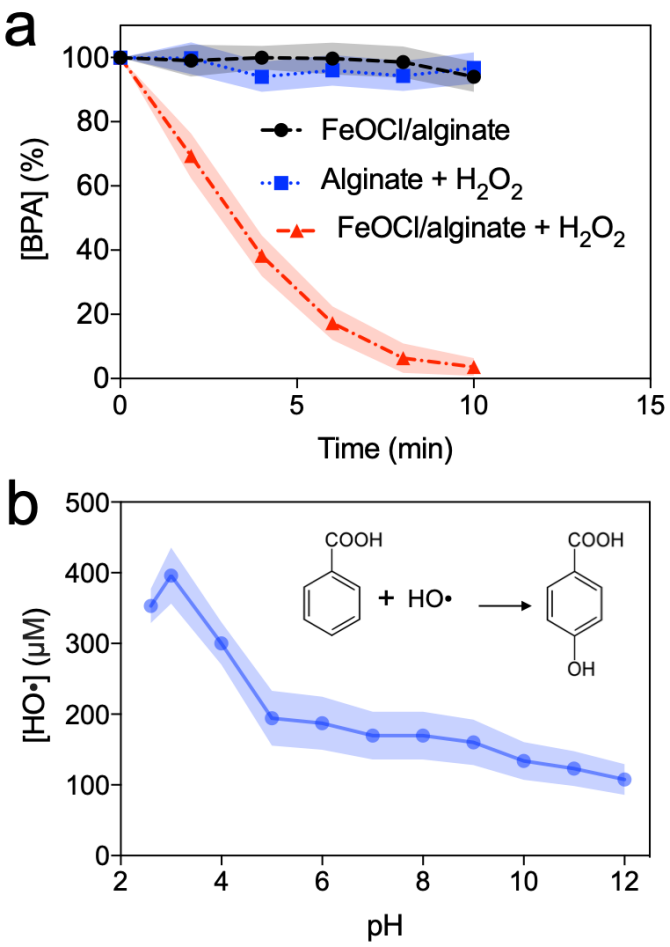

Figure S10. Activity of synthesized FeOCl/alginate. (**a**). BPA degradation by FeOCl/alginate and H_2O_2 reaction. (**b**). Quantification of generated HO• radical by FeOCl/alginate and H_2O_2 reaction at different pH. Reaction conditions: 0.075 g/mL FeOCl/alginate (dry weight), 10 mM H_2O_2. For (**a**) 10 μM BPA as substrate at pH 3, (**b**) 5 mM benzoic acid as HO• radical trapping agent at different solution pH. HO• radical was quantified after reaction for 30 min.

Note S4. At pH 3, 0.2 g/L FeOCl and 10 mM H_2O_2 mediated formation of 305.3 μM HO• radical (**Fig. S4b**) after 30 min, while 0.075 g/mL FeOCl/alginate (dry weight, 1:2 FeOCl:alginate) produced 396.2 μM HO• radical (**Fig. S10b**). As a result, the specific activity of unimmobilized and immobilized FeOCl was calculated as 1511.5 and 15.8 μM HO•/(g L^{-1}) FeOCl, respectively.

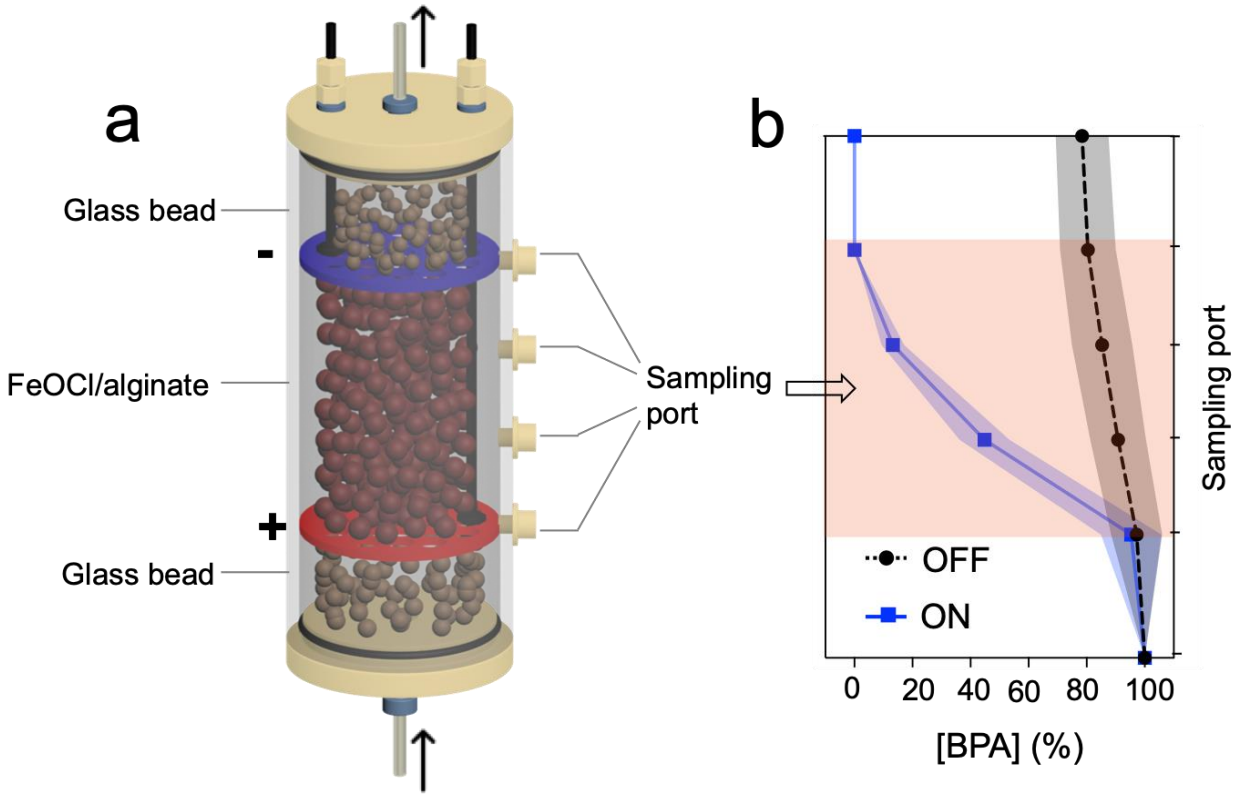

Figure S11. BPA removal by EFL platform loading FeOCl/alginate catalyst composite. (**a**). Illustration of reactor components, (**b**). BPA removals from each sampling port as the electric current was turned on and off.

Note S5. The 4.5 g (dry weight) as-prepared FeOCl/alginate was filled in between the cathode and anode, and all other spaces were filled with glass beads to reduce hydrodynamic perturbation. The pore volume of our reactor between cathode and anode was 60 mL. Typically, a neutral solution containing 10 mM H_2O_2, 10 μM BPA, and 5 mM Na_2SO_4 as electrolyte was pumped up into the vertically aligned reactor at a rate of 3 mL/min. A steady-state acidic-compartment was formed between the cathode and anode under a current of 40 mA after 60 min, and FeOCl/alginate catalyzed H_2O_2 decomposition for BPA removals was tested.

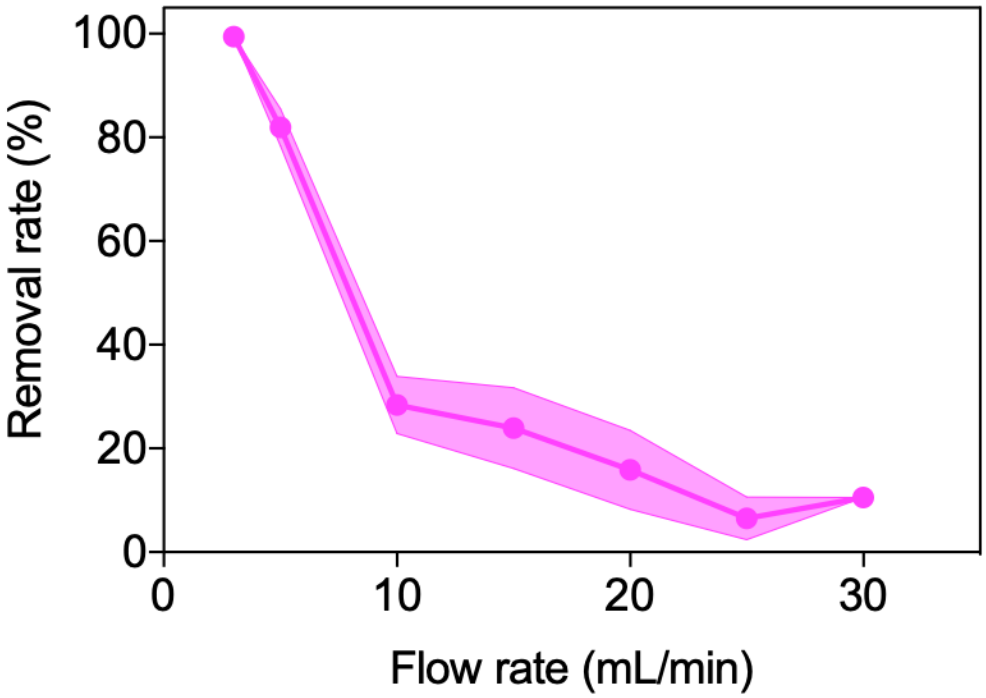

Figure S12. BPA removal under different flow rate by EFL platform loading FeOCl/alginate catalyst composite (as shown in **Fig. S11a**).

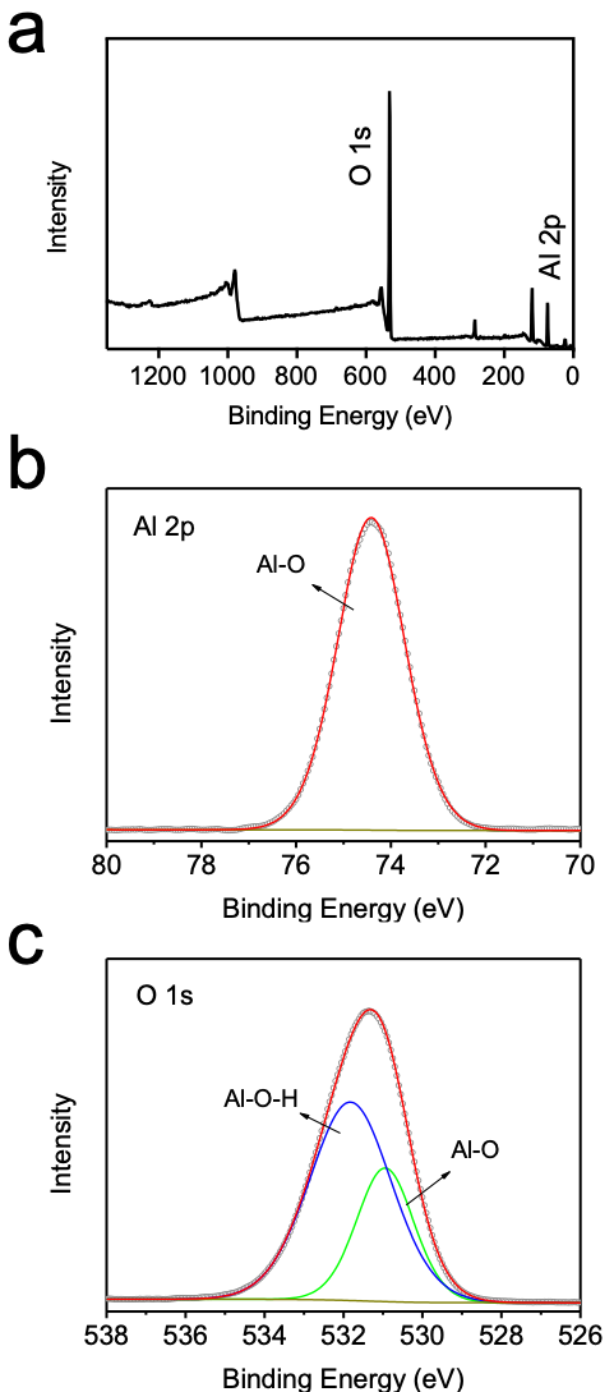

Figure S13. XPS characterization of γ-Al_2O_3. (**a**). Survey spectrum, (**b**). Al 2p, (**c**). O 1s. The observed Al-O-H bond was due to chemisorbed moisture on γ-Al_2O_3 surface.

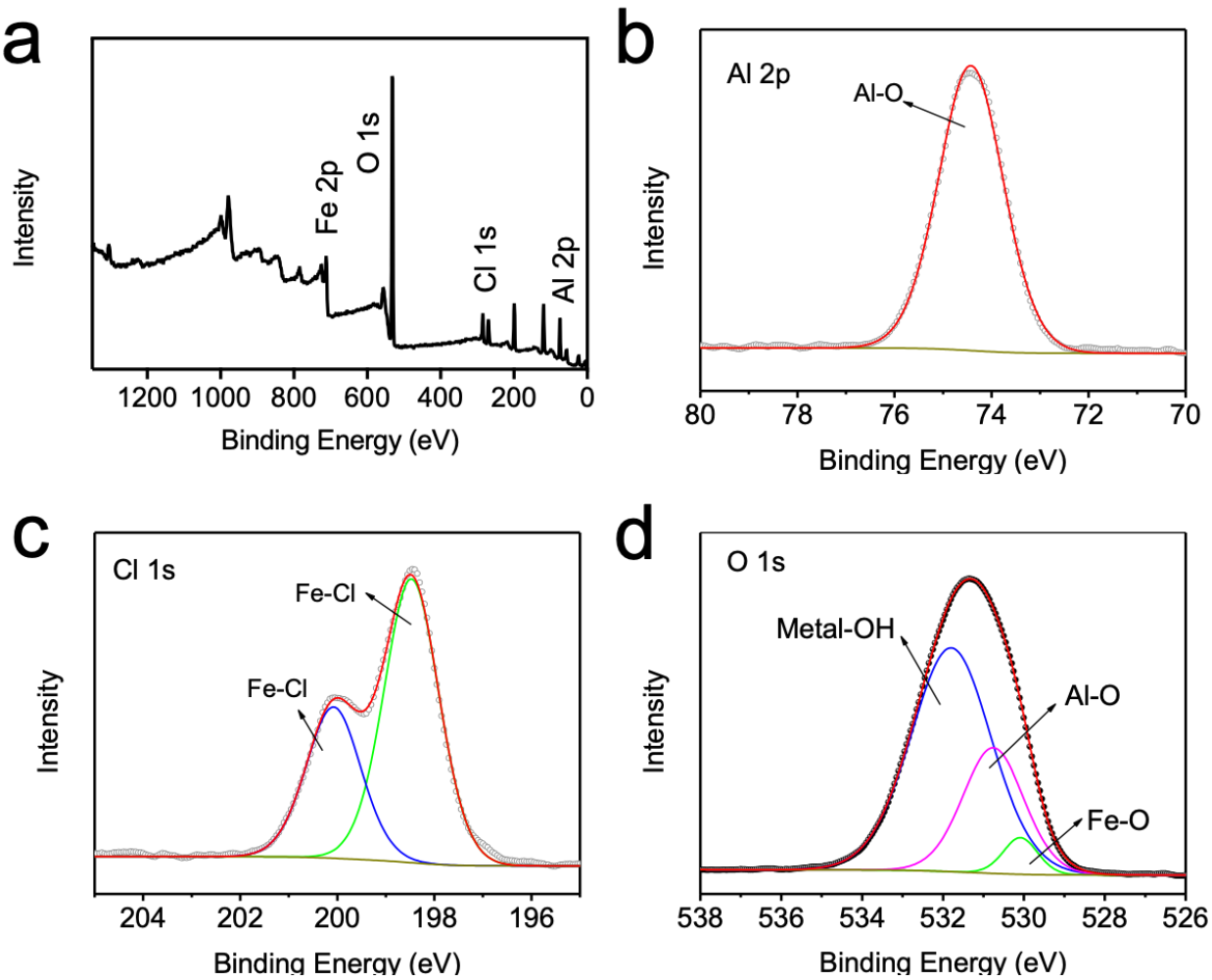

Figure S14. XPS characterization of FeOCl/Al_2O_3. (**a**). Survey spectrum, (**b**). Al 2p, (**c**). Cl 1s, (**d**). O 1s. Fe 2p deconvolution spectra are shown in **Figure 2g** in the main text.

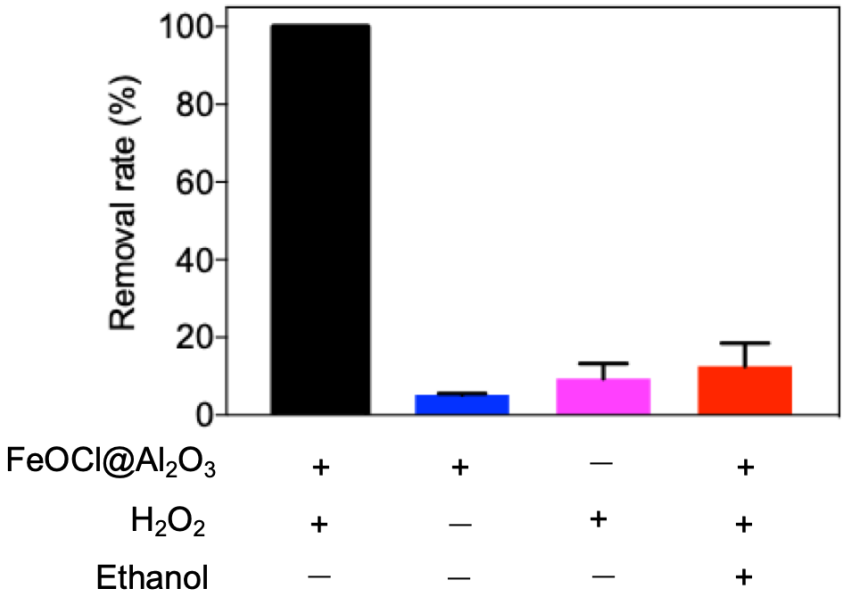

Figure S15. Control experiments of column reaction. BPA removal by the EFL water treatment platform with 1). Both $FeOCl/Al_2O_3$ and H_2O_2, 2). Only $FeOCl/Al_2O_3$, 3). Only H_2O_2, and 4). $FeOCl/Al_2O_3$, H_2O_2, and ethanol. Reaction conditions: 100 mA electric current, 15 mL/min flow rate, 10 mM H_2O_2, 5 mM Na_2SO_4 electrolyte, pH 7. When $FeOCl/Al_2O_3$ was not used, silica sand particles were filled into the catalyst zone instead. 10 mM ethanol was used as $HO^{\bullet}$ radical quencher.

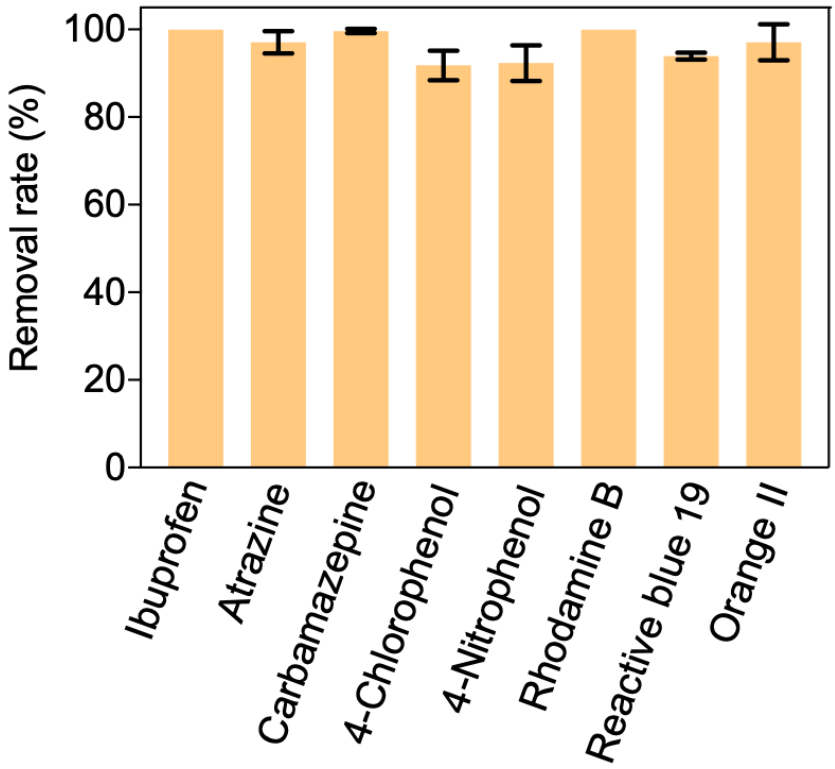

Figure S16. Degradation of recalcitrant organic contaminants by the developed electro-Fenton-like water treatment platform. Initial concentration of these compounds was 10 μM.

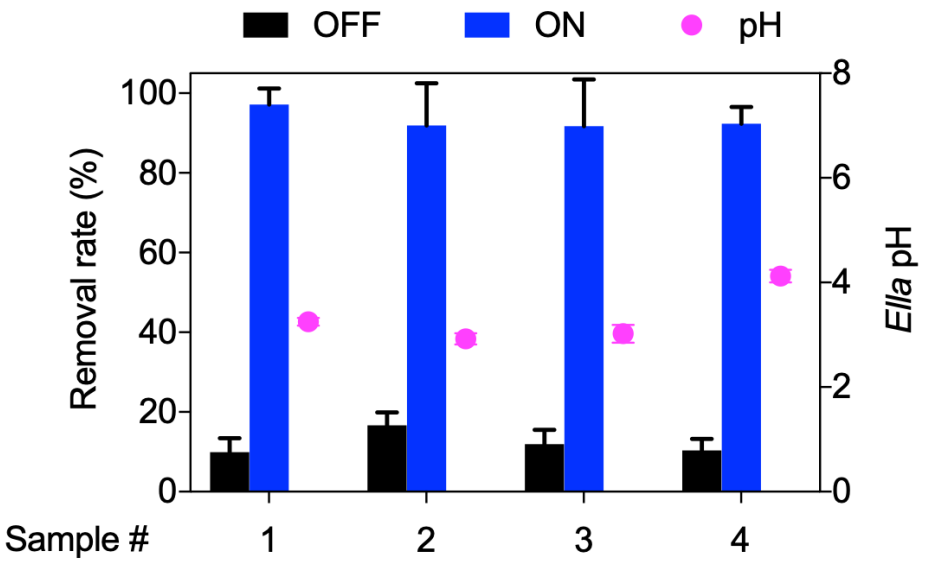

Figure S17. BPA removal by EFL platform in field water matrices. Operating condition: influent (10 mM H_2O_2 and 10 μM BPA in field water sample) was pumped into the column at 15 mL/min, and 100 mA electric current was applied to electrodes. *Ella* pH denotes the average of solution pHs from two middle sampling ports.

Table S1. Summary of heterogeneous Fenton-like catalysts owning peroxidase-mimicking functions in literature.

Catalyst	Activity	Optimum pH	Synthesis method	Reference
Horseradish peroxidase (HRP)	TMB: K_m = 0.434 mM, V_{max} = 10 × 10^{-8} M s^{-1}, k_{cat} = 0.4 × 10^4 s^{-1}; H_2O_2: K_m = 3.7 mM, V_{max} = 8.71 × 10^{-8} M s^{-1}, k_{cat} = 0.348 × 10^3 s^{-1};	4	Genetically encoded	10
Fe_3O_4	TMB: K_m = 0.098 mM, k_{cat} = 3.02 × 10^4 s^{-1}; H_2O_2: K_m = 154 mM, k_{cat} = 8.58 × 10^4 s^{-1}	3.5	Solvothermal method, co-precipitation method	10-12
$KFePW_{12}O_{40}$	TMB: K_m = 0.346 mM, V_{max} = 3.7 × 10^{-8} M s^{-1}; H_2O_2: K_m = 165 mM, V_{max} = 6.9 × 10^{-8} M s^{-1}	4.5	1) Synthesis of $K_3PW_{12}O_{40}$ through hydrothermal treatment of KCl and $H_3[PW_{12}O_{40}]$; 2) iron ion exchange with K^+	13
$H_3PW_{12}O_{40}$	TMB: K_m = 0.11 mM, V_{max} = 43.1 × 10^{-8} M s^{-1}; H_2O_2: K_m = 15.89 mM, V_{max} = 42400 × 10^{-8} M s^{-1}	3	N.A.	14
FA-Fe_2SiW_{10}	H_2O_2: K_m = 0.014 mM, V_{max} = 14.24 × 10^{-8} M s^{-1}	4	Co-precipitation method	15
V_2O_5	TMB: K_m = 0.165 mM, V_{max} = 2.4 × 10^{-8} M s^{-1}; H_2O_2: K_m = 0.058 mM, V_{max} = 1.4 × 10^{-8} M s^{-1}	4	Hydrothermal method	16
Nanoceria	TMB: K_m = 3.8 mM, V_{max} = 70 × 10^{-8} M s^{-1}	4	Solution reaction at room temperature	17
Co_3O_4	TMB: K_m = 0.037 mM, V_{max} = 6.27 × 10^{-8} M s^{-1}; H_2O_2: K_m = 140 mM, V_{max} = 12.1 × 10^{-8} M s^{-1}	6	Heating and precipitation	18
$MnFe_2O_4$	TMB: K_m = 0.112-0.543 mM, V_{max} = (3.53-69.8) × 10^{-4} M s^{-1}; H_2O_2: K_m = 0.00146-0.0964 mM, V_{max} = (5.15-71.5) × 10^{-4} M s^{-1}	3.5	Heating and precipitation	19

Ferrocene	TMB: K_m = 0.13 mM, V_{max} = 4.79 × 10^{-9} M s^{-1}, k_{cat} = 4.79 × 10^{-3} s^{-1}; H_2O_2: K_m = 50.08 mM, V_{max} = 9.77 × 10^{-9} M s^{-1}, k_{cat} = 9.77 × 10^{-3} s^{-1};	3	Commercially available	20
Ag_3PO_4	TMB: K_m = 0.327 mM, V_{max} = 2.01 × 10^{-8} M s^{-1}; H_2O_2: K_m = 0.216 mM, V_{max} = 1.27 × 10^{-8} M s^{-1}	2.5	Solution reaction at room temperature	21
Nanodiamond−gold nanocomposites	OPD: K_m = 6.4-48.7 mM, k_{cat} = 290.4-319.3 mM s^{-1} mg^{-2}; H_2O_2: K_m = 89.7-208.7 mM, k_{cat} = 377.6-565.6 mM s^{-1} mg^{-2};	N.A.	Solution reduction and heating	22
MOF-88	TMB: K_m = 0.0796 mM, V_{max} = 3.12 × 10^{-8} M s^{-1}; H_2O_2: K_m = 1.06 mM, V_{max} = 1.39 × 10^{-8} M s^{-1}	3	Heating and precipitation	23
Nitrogen-doped graphene quantum dots	TMB: K_m = 11.19 mM, V_{max} = 0.38 × 10^{-8} M s^{-1}; H_2O_2: K_m = 0.1 mM, V_{max} = 0.14 × 10^{-8} M s^{-1}	3	Acid treatment of graphene oxide	24
Carboxyl-modified graphene oxide	TMB: K_m = 0.0237 mM, V_{max} = 3.45 × 10^{-8} M s^{-1}; H_2O_2: K_m = 3.99 mM, V_{max} = 3.85 × 10^{-8} M s^{-1}	4	$KMnO_4$ oxidation of graphene oxide	25
H@M	TMB: K_m = 10.9 mM, V_{max} = 8.98 × 10^{-8} M s^{-1}; H_2O_2: K_m = 0.068 mM, V_{max} = 6.07 × 10^{-8} M s^{-1}	5	Impregnation of hemin into MOF	26
Cubic Pt nanocrystal	N.A.	3.4	Solution reduction and heating	27
Rh NS	TMB: K_m = 0.264 mM, V_{max} = 12.56 × 10^{-8} M s^{-1}, k_{cat} = 8.2 × 10^4 s^{-1}; H_2O_2: K_m = 4.51 mM, V_{max} = 68.09 × 10^{-8} M s^{-1}, k_{cat} = 44.5 × 10^4 s^{-1};	4	Solution reduction and heating	28
MoS_2 NS	TMB: K_m = 0.525 mM, V_{max} = 5.16 × 10^{-8} M s^{-1}; H_2O_2: K_m = 0.0116 mM, V_{max} = 4.29 × 10^{-8} M s^{-1}	2-7.5	Solution-based exfoliation	29
$MoSe_2$ NS	TMB: K_m = 0.014 mM, V_{max} = 0.56 × 10^{-8} M s^{-1}; H_2O_2: K_m = 0.155 mM, V_{max} = 0.99 × 10^{-8} M s^{-1}	3.5	Liquid exfoliation method	30
WS_2 NS	TMB: K_m = 1.83 mM, V_{max} = 4.31 × 10^{-8} M s^{-1}; H_2O_2: K_m = 0.24 mM, V_{max} = 4.52 × 10^{-8} M s^{-1}	2-7	Commercially available	31
WSe_2 NS	TMB: K_m = 0.0433 mM, V_{max} = 1.43 × 10^{-8} M s^{-1}; H_2O_2: K_m = 19.53 mM, V_{max} = 2.22 × 10^{-8} M s^{-1}	3.5	Liquid exfoliation method	32

ZIF-67	TMB: K_m = 13.69 mM, V_{max} = 0.35 × 10^{-8} M s^{-1}; H_2O_2: K_m = 3.52 mM, V_{max} = 0.28 × 10^{-8} M s^{-1}	< 4	Heating and precipitation	33
Cu-MOF	TMB: K_m = 4.11 mM, V_{max} = 55.56 × 10^{-8} M s^{-1}; H_2O_2: K_m = 6.41 mM, V_{max} = 10.2 × 10^{-8} M s^{-1}	4	Solution reaction at room temperature	34
Fe_2O_3	NP: K_m = 36.82 mg/L, V_{max} = 1.36 mg/min, k_{cat} = 0.273 min^{-1}	8	Solution reaction at room temperature	35
2LFh	NP: K_m = 46.67 mg/L, V_{max} = 1.17 mg/min, k_{cat} = 0.234 min^{-1}	8	Solution reaction at room temperature	35
PdCu	TMB: K_m = 0.25 mM, V_{max} = 1.19 × 10^{-8} M s^{-1}, k_{cat} = 20.2 × 10^{-5} s^{-1}; H_2O_2: K_m = 3.05 mM, V_{max} = 6.25 × 10^{-6} M s^{-1}, k_{cat} = 10.61 × 10^{-2} s^{-1};	4	Microwave-assisted wet-chemical synthetic approach	36
Co_9S_8	TMB: K_m = 1.64 mM, V_{max} = 99 × 10^{-8} M s^{-1}; H_2O_2: K_m = 7.39 mM, V_{max} = 35 × 10^{-8} M s^{-1}	3	Heating and precipitation	37
$Cu(OH)_2$ SC	TMB: K_m = 2.448 mM, V_{max} = 44.83 × 10^{-8} M s^{-1}; H_2O_2: K_m = 0.199 mM, V_{max} = 42.51 × 10^{-8} M s^{-1}	4.5	Solution reaction at room temperature	38
Ru frame	TMB: K_m = 0.0603 mM, V_{max} = 13.4 × 10^{-8} M s^{-1}; H_2O_2: K_m = 318 mM, V_{max} = 7.41 × 10^{-8} M s^{-1}	0-12	Heating and precipitation	39
FePt-Au HNP	TMB: K_m = 0.445 mM, V_{max} = 24.67 × 10^{-8} M s^{-1}; H_2O_2: K_m = 0.0185 mM, V_{max} = 0.6894 × 10^{-8} M s^{-1}	4	Hydrothermal method	40
PtAg-MoS_2	TMB: K_m = 25.71 mM, V_{max} = 7.29 × 10^{-8} M s^{-1}; H_2O_2: K_m = 0.386 mM, V_{max} = 3.22 × 10^{-8} M s^{-1}	4	Heating and precipitation	41
PtPd NP	TMB: K_m = 1.78 mM, V_{max} = 36.4 × 10^{-8} M s^{-1}; H_2O_2: K_m = 0.053 mM, V_{max} = 9.26 × 10^{-8} M s^{-1}	9.5	Reduction and mild heating	42
Cu-hemin	TMB: K_m = 1.42 mM, V_{max} = 26.22 × 10^{-8} M s^{-1}; H_2O_2: K_m = 2.18 mM, V_{max} = 116 × 10^{-8} M s^{-1}	6	Reduction and mild heating	43
PS@Au@PB	TMB: K_m = 1.22 mM, V_{max} = 59 × 10^{-8} M s^{-1}; H_2O_2: K_m = 0.17 mM, V_{max} = 38.9 × 10^{-8} M s^{-1}	5.2	Solution reaction at room temperature	44
Cu NC	TMB: K_m = 0.648 mM, V_{max} = 5.96 × 10^{-8} M s^{-1}; H_2O_2: K_m = 29.16 mM, V_{max} = 4.22 × 10^{-8} M s^{-1}	6	Solution reaction and mild heating	45

Table S2. BET (Brunauer-Emmett-Teller) characterizations of γ-Al_2O_3 support and synthesized FeOCl/Al_2O_3.

		γ-Al_2O_3	FeOCl/Al_2O_3
	BET Surface Area	883.9819 m^2/g	212.7531 m^2/g
Pore Volume	BJH Adsorption cumulative volume of pores between 1.7 nm and 300 nm width	1.396243 cm^3/g	0.577339 cm^3/g
	BJH Desorption cumulative volume of pores between 1.7 nm and 300 nm width	1.401154 cm^3/g	0.556347 cm^3/g
Pore Size	Adsorption average pore diameter (4V/A by BET)	5.92993 nm	10.94665 nm
	BJH Adsorption average pore width (4V/A)	7.8207 nm	8.7791 nm
	BJH Desorption average pore width (4V/A)	7.0510 nm	9.1477 nm

Table S3. Quantification methods of selected organic compounds.

Substrate	Detection method	Mobile phase	Ratio	Flow rate (mL/min)	Detection wavelength
Ibuprofen	HPLC	methanol/water	68/32	0.5	228 nm
Atrazine	HPLC	methanol/water	60/40	0.5	228 nm
Carbamazepine	HPLC	methanol/water	60/40	0.5	285 nm
4-Chlorophenol	HPLC	acetonitrile/water	30/70	0.5	225 nm
4-Nitrophenol	HPLC	acetonitrile/water	60/40	0.5	280 nm
Rhodamine B	UV-Vis spectrometer	—	—	—	554 nm
Reactive blue 19	UV-Vis spectrometer	—	—	—	592 nm
Orange II	UV-Vis spectrometer	—	—	—	485 nm

Table S4. Characterizations of field water samples.

Water sample	Water type	Total organic carbon (mg/L)	Dissolved oxygen (mg/L)	pH
Sample 1	Lake water	21.4	8.38	8.51
Sample 2	Lake water	115.5	7.49	8.29
Sample 3	Underground water	87.2	7.92	7.31
Sample 4	Underground water	158.7	7.21	7.78

Supplemental References:

1. De Smedt, F., and Wierenga, P.J. (1984). Solute transfer through columns of glass beads. Water Resources Res. *20*, 225-232.

2. Acar, Y.B., and Alshawabkeh, A.N. (1993). Principles of electrokinetic remediation. Environ. Sci. Technol. *27*, 2638–2647.

3. Davis, E.M., and Davis, R.J. (2003). Fundamentals of chemical reaction engineering. (McGraw-Hill Higher Education).

4. Hojabri, S., Rajic, L., and Alshawabkeh, A.N. (2018). Transient reactive transport model for physico-chemical transformation by electrochemical reactive barriers. J. Hazard. Mater. *358*, 171-177.

5. Paz-García, J.M., Villén-Guzmán, M., García-Rubio, A., Hall, S., Ristinmaa, M., and César, G.L. (2016). A coupled reactive-transport model for electrokinetic remediation. In Electrokinetics Across Disciplines and Continents, Ribeiro, A.B., Mateus, E.P., and Couto, N. (Springer International Publishing), pp. 251–278.

6. Steefel, C.I., and Lasaga, A.C. (1994). A coupled model for transport of multiple chemical species and kinetic precipitation/dissolution reactions with application to reactive flow in single phase hydrothermal systems. Am. J. Sci. *294*, 529-592.

7. Parkhurst, D.L., and Appelo, C.A.J. (2013). PHREEQC (version 3)-a computer program for speciation, batch-reaction, one-dimensional transport, and inverse geochemical calculations. In Modeling Techniques, p. 497.

8. Nardi, A., Idiart, A., Trinchero, P., De Vries, L. M., and Molinero, J. (2014). Interface COMSOL-PHREEQC (iCP), an efficient numerical framework for the solution of coupled multiphysics and geochemistry. Comput. Geosci. *69*, 10–21.

9. Versteeg, H.K., and Malalasekera, W. (2007). An introduction to computational fluid dynamics: the finite volume method. (Pearson Education).

10. Gao, L., Zhuang, J., Nie, L., Zhang, J., Zhang, Y., Gu, N., Wang, T., Feng, J., Yang, D., Perrett, S., and Yan, X. (2007). Intrinsic peroxidase-like activity of ferromagnetic nanoparticles. Nat. Nanotechnol. *2*, 577-583.

11. Deng, H., Li, X., Peng, Q., Wang, X., Chen, J., and Li. Y. (2005). Monodisperse magnetic single-crystal ferrite microspheres. Angew. Chem. Int. Ed. *44*, 2782–2785.

12. Ma, M., Wu, Y., Zhou, J., Sun, Y., Zhang, Y., and Gu, N. (2004). Size dependence of specific power absorption of Fe_3O_4 particles in AC magnetic field. J. Magn. Magn. Mater. *268*, 33–39.

13. Zeb, A., Sahar, S., Qazi, U.Y., Odda, A.H., Ullah, N., Liu, Y., Qazi, I.A., and Xu, A.W. (2018). Intrinsic peroxidase-like activity and enhanced photo-Fenton reactivity of iron-substituted polyoxometallate nanostructures. Dalton Trans. *47*, 7344-7352.

14. Wang, J., Han, D., Wang, X., Qi, B., and Zhao, M. (2012). Polyoxometalates as peroxidase mimetics and their applications in H_2O_2 and glucose detection. Biosens. Bioelectron. *36*, 18-21.

15. Sun, C., Chen, X., Xu, J., Wei, M., Wang, J., Mi, X., Wang, X., Wu, Y., and Liu, Y. (2013). Fabrication of an inorganic–organic hybrid based on an iron-substituted polyoxotungstate as a peroxidase for colorimetric immunoassays of H_2O_2 and cancer cells. J. Mater. Chem. A *1*, 4699-4705.

16. Qu, K., Shi, P., Ren, J., and Qu, X. (2014). Nanocomposite incorporating V_2O_5 nanowires and gold nanoparticles for mimicking an enzyme cascade reaction and its application in the detection of biomolecules. Chem.: Eur. J. *20*, 7501-7506.

17. Asati, A., Santra, S., Kaittanis, C., Nath, S., and Perez, J.M. (2009). Oxidase-like activity of polymer-coated cerium oxide nanoparticles. Angew. Chem. Int. Ed. *121*, 2344-2348.

18. Mu, J., Wang, Y., Zhao, M., and Zhang, L. (2012). Intrinsic peroxidase-like activity and catalase-like activity of Co_3O_4 nanoparticles. Chem. Comm. *48*, 2540-2542.

19. Peng, Y., Wang, Z., Liu, W., Zhang, H., Zuo, W., Tang, H., Chen, F., and Wang, B. (2015). Size-and shape-dependent peroxidase-like catalytic activity of $MnFe_2O_4$ nanoparticles and their applications in highly efficient colorimetric detection of target cancer cells. Dalton Trans. *44*, 12871-12877.

20. Wang, Q., Ma, K., Yu, Z., Ding, J., Hu, Q., Liu, Q., Sun, H., Wen, D., Liu Q., and Kong, J. (2018). The peroxidase-like catalytic activity of ferrocene and its application in the biomimetic synthesis of microsphere polyaniline. New J. Chem. *42*, 13536-13540.

21. Liu, Y., Zhu, G., Yang, J., Yuan, A., and Shen, X. (2014). Peroxidase-like catalytic activity of Ag_3PO_4 nanocrystals prepared by a colloidal route. PloS one *9*, e109158.

22. Kim, M. C., Lee, D., Jeong, S.H., Lee, S.Y., and Kang, E. (2016). Nanodiamond–gold nanocomposites with the peroxidase-like oxidative catalytic activity. ACS Appl. Mater. Interfaces *8*, 34317-34326.

23. Zheng, H., Liu, C., Zeng, X., Chen, J., Lü, J., Lin, R., Cao, R., Lin, Z., and Su, J. (2018). MOF-808: A metal–organic framework with intrinsic peroxidase-like catalytic activity at neutral pH for colorimetric biosensing. Inorg. Chem. *57*, 9096-9104.

24. Lin, L., Song, X., Chen, Y., Rong, M., Zhao, T., Wang, Y., Jiang, Y., and Chen, X. (2015). Intrinsic peroxidase-like catalytic activity of nitrogen-doped graphene quantum dots and their application in the colorimetric detection of H_2O_2 and glucose. Anal. Chim. Acta *869*, 89-95.

25. Song, Y., Qu, K., Zhao, C., Ren, J., and Qu, X. (2010). Graphene oxide: intrinsic peroxidase catalytic activity and its application to glucose detection. Adv. Mater. *22*, 2206-2210.

26. Qin, F., Jia, S., Wang, F., Wu, S., Song, J., and Yong Liu. (2013). Hemin@metal–organic framework with peroxidase-like activity and its application to glucose detection. Catal. Sci. Technol. *3*, 2761-2768.

27. Ma, M., Zhang, Y., and Gu, N. (2011). Peroxidase-like catalytic activity of cubic Pt nanocrystals. Colloids Surf. A *373*, 6-10.

28. Cai, S., Xiao, W., Duan, H., Liang, X., Wang, C., Yang, R., and Li, Y. (2018). Single-layer Rh nanosheets with ultrahigh peroxidase-like activity for colorimetric biosensing. Nano Res. *11*, 6304-6315.

29. Lin, T., Zhong, L., Guo, L., Fu, F., and Chen, G. (2014). Seeing diabetes: visual detection of glucose based on the intrinsic peroxidase-like activity of MoS_2 nanosheets. Nanoscale *6*, 11856-11862.

30. Wu, X., Chen, T., Wang, J., and Yang, G. (2018). Few-layered $MoSe_2$ nanosheets as an efficient peroxidase nanozyme for highly sensitive colorimetric detection of H_2O_2 and xanthine. J. Mater. Chem. B *6*, 105-111.

31. Lin, T., Zhong, L., Song, Z., Guo, L., Wu, H., Guo, Q., Chen, Y., Fu, F., and Chen, G. (2014). Visual detection of blood glucose based on peroxidase-like activity of WS_2 nanosheets. Biosens. Bioelectron. *62*, 302-307.

32. Chen, T.M., Wu, X.J., Wang, J.X., and Yang, G.W. (2017). WSe_2 few layers with enzyme mimic activity for high-sensitive and high-selective visual detection of glucose. Nanoscale *9*, 11806-11813.

33. Wang, S., Xu, D., Ma, L., Qiu, J., Wang, X., Dong, Q., Zhang, Q., Pan, J., and Liu, Q. (2018). Ultrathin ZIF-67 nanosheets as a colorimetric biosensing platform for peroxidase-like catalysis. Anal. Bioanal. Chem. *410*, 7145-7152.

34. Wang, C., Gao, J., and Tan, H. (2018). Integrated antibody with catalytic metal–organic framework for colorimetric immunoassay. ACS Appl. Mater. Interfaces *10*, 25113-25120.

35. Pariona, N., Herrera-Trejo, M., Oliva, J., and Martinez, A.I. (2016). Peroxidase-like activity of ferrihydrite and hematite nanoparticles for the degradation of methylene blue. J. Nanomater. *2016*, 3427809.

36. He, Y., Niu, X., Li, L., Li, X., Zhang, W., Zhao, H., Lan, M., Pan, J., and Zhang. X. (2018). Microwave-assisted fabrication of bimetallic PdCu nanocorals with enhanced peroxidase-like activity and efficiency for thiocyanate sensing. ACS Appl. Nano Mater. *1*, 2397-2405.

37. Mu, J., Li, J., Zhao, X., Yang, E.C., and Zhao, X.J. (2018). Novel urchin-like Co_9S_8 nanomaterials with efficient intrinsic peroxidase-like activity for colorimetric sensing of copper(II) ion. Sensor. Actuat. B: Chem. *258*, 32-41.

38. Cai, R., Yang, D., Peng, S., Chen, X., Huang, Y., Liu, Y., Hou, W., Yang, S., Liu, Z., and Tan, W. (2015). Single nanoparticle to 3D supercage: framing for an artificial enzyme system. J. Am. Chem. Soc. *137*, 13957-13963.

39. Ye, H., Mohar, J., Wang, Q., Catalano, M., Kim, M.J., and Xia, X. (2016). Peroxidase-like properties of ruthenium nanoframes. Sci. Bull. *61*, 1739-1745.

40. Ding, Y., Yang, B., Liu, H. Liu, Z., Zhang, X., Zheng, X., and Liu. Q. (2018). FePt-Au ternary metallic nanoparticles with the enhanced peroxidase-like activity for ultrafast colorimetric detection of H_2O_2. Sensor. Actuat. B: Chem. *259*, 775-783.

41. Cai, S., Han, Q., Qi, C., Lian, Z., Jia, X., Yang, R., and Wang, C. (2016). $Pt_{74}Ag_{26}$ nanoparticle-decorated ultrathin MoS_2 nanosheets as novel peroxidase mimics for highly selective colorimetric detection of H_2O_2 and glucose. Nanoscale *8*, 3685-3693.

42. Jiang, T., Song, Y., Du, D., Liu, X., and Lin, Y. (2016). Detection of p53 protein based on mesoporous Pt–Pd nanoparticles with enhanced peroxidase-like catalysis. ACS Sensors *1*, 717-724.

43. Liu, F., He, J., Zeng, M., Hao, J., Guo, Q., Song, Y. and Wang, L. (2016). Cu–hemin metal-organic frameworks with peroxidase-like activity as peroxidase mimics for colorimetric sensing of glucose. J. Nanopart. Res. *18*, 106.

44. Zhang, X.Z., Zhou, Y., Zhang, W., Zhang, Y., and Gu, N. (2016). Polystyrene@Au@prussian blue nanocomposites with enzyme-like activity and their application in glucose detection. Colloids Surf. A *490*, 291-299.

45. Hu, L., Yuan, Y., Zhang, L., Zhao, J., Majeed, S., Xu, G. (2013). Copper nanoclusters as peroxidase mimetics and their applications to H_2O_2 and glucose detection. Anal. Chim. Acta *762*, 83-86.